Internal tides off the Amazon shelf Part I: importance for the structuring of ocean temperature during two contrasted seasons

Fernand Assene[1], Ariane Koch-Larrouy[2], Isabelle Dadou[3], Michel Tchilibou[4], Guillaume Morvan[5], Jérôme Chanut[6], Alex Costa da Silva[7], Vincent Vantrepotte[8], Damien Allain[9], Trung-Kien Tran[10]

[1, 2, 3, 5, 9]Université de Toulouse, LEGOS (CNES/CNRS/IRD/UT3), Toulouse, France
[1, 6]Mercator Ocean International, 31400, Toulouse, France
[4]Collecte Localisation Satellites (CLS), 31500, Ramonville Saint-Agne, France
[7]Departamento de Oceanografia da Universidade Federal de Pernambuco, DOCEAN/UFPE, Recife, Brazil
[8, 10]Laboratoire d'Océanologie et de Géosciences (LOG), 62930, Wiméreux, France

Correspondence to: Fernand Assene (*fassene@mercator-ocean.fr*)

Abstract

The impact of internal and barotropic tides on the vertical and horizontal temperature structure off the Amazon River was investigated during two highly contrasted seasons (AMJ: April-May-June and ASO: August-September-October) over a three-year period from 2013 to 2015. Twin regional simulations, with and without tides, were used to highlight the general effect of tides. The findings reveal that tides have a cooling effect on the ocean from the surface (~0.3 °C) to above the thermocline (~1.2 °C), while warming it up below the thermocline (~1.2 °C). The heat budget analysis indicates that the vertical mixing is the dominant process driving temperature variations within the mixed layer, while it is associated with both horizontal and vertical advection to explain temperature variations below. The increased mixing in the simulations including tides is attributed to breaking of internal tides (IT) on their generation sites over the shelf break and offshore along their propagation pathways. Over the shelf, mixing is driven by the dissipation of the barotropic tides. In addition, the vertical terms of the heat budget equation exhibit wavelength patterns typical of mode-1 IT. The study highlights the key role of tides and particularly how IT-related vertical mixing shapes the ocean temperature off the Amazon. Furthermore, we found that tides impact the interactions between the upper ocean interface and the overlying atmosphere. They contribute significantly to increasing the net heat flux between the atmosphere and the ocean, with a notable seasonal variation from 33.2% in AMJ to 7.4% in ASO seasons. This emphasizes the critical role of tidal dynamics in understanding regional-scale climate.

Keywords: Amazon shelf break, modeling, internal tides, mixing, cooling, heat flux.

I. Introduction

In the ocean, many processes depend on temperature. These processes include water mass formation (Swift and Aagaard, 1981; Lascaratos, 1993; Speer et al., 1995), the transport and mixing of tracers, exchanges with other biosphere compartments (Archer et al., 2004, Rosenthal et al., 1997), and, most importantly, surface heat exchange at the interface with the atmosphere (Clayson and Bogdanoff, 2013; Mei et al., 2015), which significantly influence the climate (Li et al., 2006; Collins et al., 2010). The oceanic thermal structure can be modified at various spatial and temporal scales through external processes such as solar radiation, heat exchanges with the atmosphere, winds, precipitation, and freshwater inputs from rivers, as well as internal processes including mass transport by currents and eddies (e.g., Aguedjou et al., 2021), mixing by turbulent diffusion (Kunze et al., 2012), and the dissipation of internal waves (Barton et al., 2001; Smith et al., 2004; Salamena et al., 2021). Additionally, bottom friction of barotropic tidal currents can lead to intensified mixing, particularly in shallow water conditions over a shelf (see Lambeck and Runcorn, 1977; Le Provost and Lyard, 1997), and significantly modify ocean temperature in surface layers (Li et al., 2020).

The barotropic tides, also called external tides, serve as the primary source for generating internal waves. When barotropic tides interact with sharp topography such as ridge, sea mounts, shelf break in a stratified ocean, they generate internal tides (IT) that propagate and dissipate in the ocean interior causing diapycnal mixing (Baines, 1982; Munk and Wunsch, 1998; Egbert and Ray, 2000). Several observational and modelling studies have demonstrated that this dissipation occurs at the generation sites, through reflection at the ocean bottom, or near the surface when the energy rays interact with the pycnocline (among others: Laurent and Garrett, 2002; Sharples et al., 2007, 2009; Koch-Larrouy et al., 2015; Nugroho et al., 2018; Whalen et al., 2012). IT also dissipate or lose energy through wave-wave interactions or when they interact with mesoscale or fine-scale structures (Vlasenko and Stashchuk, 2006; Dunphy and Lamb, 2014).

The role of IT in shaping the ocean's thermal structure has garnered increasing interest and has been the focus of numerous studies in recent years. In the shallow shelf surface waters of Hawaii, Smith et al. (2016) reported that IT can induce surface cooling ranging from 1–5 °C. Similarly, in the Indonesian region, studies by Koch-Larrouy et al. (2007, 2008), Nagai and Hibiya (2015) and Nugroho et al. (2018) found that IT lead to an average surface cooling of 0.5 °C, which subsequently reduces local atmospheric convection and results in a 20% decrease in precipitation. Therefore, IT play a significant role in the regional climate dynamics (Koch-

69   Larrouy et al., 2010; Sprintall et al., 2014, 2019). Furthermore, Jithin and Francis (2020)
70   demonstrated that in the Andaman Sea, IT can influence the temperature of deep waters (> 1600
71   m), resulting in a warming effect of about 1–2 °C. However, the impact of IT on temperature
72   off the Amazon plateau is still not well understood.

73   Our study focuses on the oceanic region of northern Brazil off the Amazon River. This
74   region experiences variations in wind patterns and hence the position of the Intertropical
75   Convergence Zone (ITCZ) throughout the year. These variations directly impact the discharge
76   of the Amazon River, oceanic circulation, eddy kinetic energy (EKE) and stratification (Muller-
77   Karger et al., 1988; Johns et al., 1990; Xie and Carton, 2004). Consequently, two contrasted
78   seasons emerge: April-May-June (AMJ) and August-September-October (ASO). The AMJ (vs.
79   ASO) season features an increasing (vs. decreasing) river discharge, there is a stronger (vs.
80   weaker) and shallower (vs. deeper) pycnocline, while the North Brazilian Current (NBC) and
81   EKE are weaker (vs. stronger) (Aguedjou et al., 2019, Tchilibou et al., 2022). During AMJ
82   season, NBC forms a weak equatorial retroflection that contributes to the Equatorial Under-
83   Current. In the ASO season, when NBC strengthens, it forms a stronger retroflection in the
84   northwest, which feeds the North Equatorial Counter Current and transports water masses
85   eastwards into the tropical Atlantic. This intensified retroflection gives rise to large anticyclonic
86   eddies called NBC Rings, which can exceed 450 km in diameter (Didden and Schott, 1993;
87   Richardson et al., 1994; Garzoli et al., 2003). These eddies play a role in transporting water
88   masses towards the Northern Hemisphere (Bourles et al., 1999; Johns et al., 1998; Schott et al.,
89   2003).

90   In this region, IT are generated at the sharp shelf break, where the depth decreases from
91   200–2000 m over few tens of kilometers (Fig.1). Six main sites (A to F) have been identified,
92   with the most intense sites, A and B, located in the southern part of the region (Fig.1; Magalhaes
93   et al., 2016, Tchilibou et al., 2022). Previous studies have indicated that the propagation of IT
94   in this region is modulated by seasonal variation in currents (Magalhaes et al., 2016; Lentini et
95   al., 2016; Tchilibou et al., 2022). Moreover, changes in stratification throughout different
96   seasons affect the activity of internal tides. In AMJ (vs. ASO) season, there is a stronger (vs.
97   smaller) energy conversion and a stronger (vs. smaller) local dissipation of IT energy (Barbot
98   et al., 2021, Tchilibou et al., 2022). The interaction between the weaker (vs. stronger)
99   background circulation and IT results in fewer (vs. more) incoherent or non-stationary internal
100   tides (Tchilibou et al., 2022).

101   During the ASO season, cold water with temperature below 27.6 °C, associated with

102   the western extension of the Atlantic Cold-water Tongue (ACT), flows into the region from the

103   south and runs along the edge of the continental shelf up to 3°N, forming a cold cell known as

104   seasonal upwelling (Lentz and Limeburner, 1995; Neto and da Silva, 2014). Based on *in situ*

105   observations, the latter suggest that this cooling is backed by the vertical advection triggered by

106   the NBC. Alternatively, Ruault et al. (2020) conducted a modeling study, comparing

107   simulations with and without tides, and demonstrated that the inclusion of tides resulted in a

108   more realistic cooling effect on this upwelling. However, it remains unclear whether the cooling

109   is a result of mixing on the shelf caused by barotropic tides or mixing caused by baroclinic tides

110   at their generation sites and propagation pathways.

111   To answer the previous questions, we use a high-resolution model (1/36°) with and

112   without explicit tidal forcing and a satellite SST product. Our aim is to examine the impact of

113   tides on the temperature structure and quantify the associated processes for the two contrasted

114   seasons (AMJ and ASO) described above. Section II provides a description of the SST product,

115   our model, and the methods used. The validation of tidal characteristics, as well as the

116   temperature is presented in section III. Section IV focuses on the analysis of the impacts of tides

117   on the temperature structure and the associated processes, as well as the influence of tides on

118   heat exchange at the atmosphere-ocean interface. The discussion and summary of the obtained

119   results are presented in sections V and VI, respectively.

II.   Data and Methods

II.1. Satellite Data: TMI SST

122   This dataset is derived from Tropical Rainfall Measurement Mission (TRMM), which

123   performs measurements using onboard TRMM Microwave Imager (TMI). The microwaves can

124   penetrate clouds and are therefore crucially important for data acquisition in low latitude

125   regions, cloudy covered during long periods of raining seasons. We use TMI data products v7.1,

126   which is the most recent version of TMI SST. It contains a daily mean of SST with a

127   0.25°×0.25° grid resolution (~25 km). This SST is obtained through inter-calibration of TMI

128   data with other microwave radiometers. The TMI SST full description and inter-calibration

129   algorithm are detailed in Wentz (2015).

II.2. The NEMO Model: *AMAZON36* configuration

131   The numerical model used in this study is the Nucleus for European Modelling of the

132   Ocean (NEMO v4.0.2, Madec et al., 2019). The specific configuration designed for this study

133 is called *AMAZON36* and covers the western tropical Atlantic region from the Amazon River

134 mouth to the open ocean. Other configurations in this region either have a coarse grid (¼° ,

135 Hernandez et al., 2016) or, when the grid is fine (1/36°), do not extend far enough eastwards

136 and exclude most of the site B (Ruault et al., 2020). The current AMAZON36 configuration

137 overcomes these limitations. The grid resolution is 1/36°, and the domain spans between

138 54.7°W–35.3°W and 5.5°S–10°N (Fig.1). In this way, we capture the internal tides radiating

139 from all the generating sites on the Brazilian shelf break. The vertical grid consists of 75

140 vertically fixed z-coordinates levels, with a narrower grid refinement near the surface,

141 comprising 23 levels in the first 100 m, whereas cell thickness reaches 160 m near the bottom.

142 The horizontal and vertical resolutions of the grid are therefore fine enough to resolve low-

143 mode IT. This grid resolution has been previously used for similar purpose in this region (e.g.,

144 Tchilibou et al., 2022).

145 A third order upstream biased scheme (UP3) with built-in diffusion is used for

146 momentum advection, while tracer advection relies on a 2nd order Flux Corrected Transport

147 (FCT) scheme (Zalesak, 1979). A Laplacian isopycnal diffusion with a constant coefficient of

148 $20\ m^2.s^{-1}$ is used for tracers. The temporal integration is achieved thanks to a leapfrog scheme

149 combined with an Asselin filter to damp numerical modes, with a baroclinic time step of 150 s.

150 The k-ε turbulent closure scheme is used for vertical diffusion. Bottom friction is quadratic

151 with a bottom drag coefficient of 2.5×10^{-3}, while lateral wall free-slip boundary conditions are

152 prescribed. A time splitting technique is used to resolve the free surface, with the barotropic

153 part of the dynamical equations integrated explicitly.

154 We use the 2020 release of the General Bathymetric Chart of the Oceans, which has

155 been interpolated onto the model's horizontal grid, with the minimal depth set to 12.8 m. The

156 model is forced at the surface by the ERA-5 atmospheric reanalysis (Hersbach et al., 2020).

157 River runoff are based on monthly means from hydrology simulation of the Interaction Sol-

158 Biosphère-Atmosphère model (ISBA, https://www.umr-cnrm.fr/spip.php?article146&lang=en)

159 and are prescribed as surface mass sources with null salinity. We use 90% of ISBA runoff based

160 on a comparison with the HYBAM runoff timeseries (http://www.ore-hybam.org). The model

161 is forced at its open boundaries by the fifteen major tidal constituents (M_2, S_2, N_2, K_2, $2N_2$,

162 MU_2, NU_2, L_2, T_2, K_1, O_1, Q_1, P_1, S_1, and M_4) and barotropic currents, derived from FES2014

163 atlas (Lyard et al., 2021). In addition, we prescribe to the open boundaries the temperature,

164 salinity, sea level, current velocity and derived baroclinic velocity from the recent

165 MERCATOR-GLORYS12 v1 assimilation data (Lellouche et al., 2018).

166   The simulations were initialized on January 1, 2005 and ran for 11 years until December
167   2015. It was found that the model achieved a seasonal cycle equilibrium after two years.
168   However, for this study, our focus lies on a three-year period from January 2013 to December
169   2015. To highlight the influence of tides on the temperature structure, we use a twin model
170   configuration without tidal forcing.

II.3. Methods

II.3.1. Tide energy budget

173   We follow Kelly et al. (2010) to separate barotropic and baroclinic tide constituents.
174   There is no separation following vertical modes, then we analyze the total energy for all the
175   resolved propagation modes for a given tidal frequency. Note that the barotropic/baroclinic tide
176   separation is performed directly by the model for better accuracy. We have only analyzed the
177   M_2 harmonic which is the major tidal constituent in this region (Prestes et al., 2018; Fassoni-
178   Andrade et al., 2023), representing ~70% of the tidal energy (Beardsley et al., 1995; Gabioux
179   et al., 2005).

180   The energy budget equations of barotropic and baroclinic tides are obtained assuming
181   that the energy tendency, the nonlinear advection and the forcing terms are small (Wang et al.,
182   2016). The remaining equations are reduced to the balance between the energy dissipation, the
183   divergence of the energy flux, and the energy conversion from barotropic to baroclinic (e.g.,
184   Buijsman et al., 2017; Tchilibou et al., 2018, 2020; Jithin and Francis, 2020; Peng et al., 2021)
185   :

$$D_{bt} + \nabla_h \cdot F_{bt} + C \approx 0 \qquad (1)$$

$$D_{bc} + \nabla_h \cdot F_{bc} - C \approx 0 \qquad (2)$$

188   bt and bc indicate the barotropic and baroclinic terms, respectively, D is the depth-integrated
189   energy dissipation, which can be understood as a proxy of the real dissipation since D may
190   encompass the energy loss of non-linear terms and/or numerical dissipation (see Nugroho et al.,
191   2018), $\nabla_h \cdot F$ represents the divergence of the depth-integrated energy flux, while C is the
192   depth-integrated barotropic-to-baroclinic energy conversion, i.e., the amount of incoming
193   barotropic energy converted into internal tides energy over the steep topography, with:

$$C = \langle \nabla H \cdot U_{bt} P_{bc}^* \rangle \qquad (3)$$

$$F_{bt} = \langle U_{bt} P_{bt} \rangle \qquad (4)$$

$$F_{bc} = \int_H^\eta \langle U_{bc} \, P_{bc} \rangle \, d_z \qquad (5)$$

196

197 where the angle bracket $\langle \cdot \rangle$ denotes the average over a tidal period, ∇H is the slope of the

198 bathymetry, U is the current velocity, P_{bc}^* is the baroclinic pressure perturbation at the bottom,

199 H is the bottom depth, η the surface elevation, P is the pressure, then F is the energy flux and

200 indicates the path of tides.

II.3.2. 3-D heat budget equation for temperature

202 The three-dimensional temperature budget was computed online and further analyzed.

203 It is the balance between the total temperature trend and the sum of the temperature advection,

204 diffusion and solar radiative and non-solar radiative fluxes (e.g., Jouanno et al., 2011;

205 Hernandez et al., 2017). The three-dimensional heat budget equation for temperature is

206 expressed as follows:

$$\partial_t T = \underbrace{-u\partial_x T - v\partial_y T - w\partial_z T}_{ADV} + LDF - \underbrace{\partial_z(K_z\partial_z T)}_{ZDF} + Forcing + Asselin \qquad (6)$$

208 here T is the model potential temperature, *(u, v, w)* are the velocity components in the (x, y, z)

209 [respectively eastward, northward and upward] directions, ADV *is* the 3-D tendency term from

210 the advection routine of the NEMO code (left to right: zonal, meridional and vertical terms).

211 Note that in our model, ADV includes some diffusivity of the temperature due to numerical

212 dissipation of the FCT advection scheme (Zalesak, 1979) in contrast to some non-diffusive

213 advection scheme like in Leclair and Madec (2009). In previous studies, for lower resolution

214 (1/4°), this mixing has been quantified to be responsible for 30% of the dissipation as part of

215 the high-frequency effect of the diffusion (Koch-Larrouy et al., 2008). We expect here at 1/36°

216 resolution that this effect will be smaller but still non negligible. Note that explicit separation

217 of this effect is beyond the scope of our study. Furthermore, tides are primarily linear in surface

218 water, however, non-linear effects intensify due to bottom friction for barotropic tides or as a

219 result of IT breaking. Consequently, we anticipate a corresponding increase in ADV. ZDF

220 denotes the vertical diffusion, LDF is the lateral diffusion, $Forcing$ is the sum of tendency of

221 temperature due to penetrative solar radiation, which includes a vertical decaying structure, and

222 the non-solar heat flux (sum of the latent, sensible, and net infrared fluxes) at the surface layer,

223 and *Asselin* corresponds to the numerical diffusion for the temperature.

III. Model validation

In this section, we assess the quality of our simulations by verifying whether they are in good agreement with the observations and other reference data. Firstly, for the barotropic and baroclinic characteristics of the M_2 tides for the year 2015, and finally for the temperature from 2013 to 2015.

III.1. M_2 Tides in the model

We initially examined the barotropic SSH and there is a good agreement in both amplitude and phase between FES2014 and the model, Fig.2a and Fig.2b, respectively. However, near the coast, few differences in amplitude are observed. The model's SSH amplitude is lower (~50 cm) north of the mouth of the Amazon, while it overestimates the amplitude by ~20 cm and ~40 cm, respectively, shoreward and on the southern part of the mouth. These biases are of a similar magnitude as those reported in Ruault et al. (2020). The flux of the barotropic tidal energy flowing inshore is depicted in Fig.2c and Fig.2d for FES2014 and the model, respectively. A portion of this energy is converted into baroclinic tidal energy over the steep slope of the bathymetry. We compared the depth-integrated barotropic-to-baroclinic energy conversion rate (C) between FES2014 and the model, Fig.2c and Fig.2d, respectively. The model successfully reproduces the same conversion patterns of FES2014 over the slope, but less offshore between 42°W–35°W and 7°N–10°N. As a result, our model overall underestimates C by approximately 30%. Niwa and Hibiya (2011) demonstrated that C increases with higher bathymetry resolution, indicating that there is more conversion with the FES2014 grid (~1.5 km) compared to our grid (~3 km).

Another portion of the barotropic energy is dissipated on the shelf through bottom friction, leading to mixing from the bottom (Beardsley et al., 1995; Gabioux et al., 2005; Bessières, 2007; Fontes et al. 2008). Most of the dissipation of barotropic energy (D_{bt}) occurs in the middle and inner shelf between 3°S–4°N with a mean value of about 0.25 W.m^{-2} (Fig.2e). The location of this dissipation aligns well with previous studies of Beardsley et al. (1995) and Bessières (2007). The remaining barotropic energy propagates over hundreds of kilometers into the estuarine systems of this region (Kosuth et al., 2009; Fassoni-Andrade et al., 2023).

The energy flux of IT (F_{bc}) indicates that they propagate from the slope towards the open ocean (Fig.2f). F_{bc} indicates the existence of six main sites of IT generation on the slope, with sites A and B being particularly significant in terms of their higher and far extended energy

flux, in good agreement with previous studies (Magalhaes et al., 2016; Barbot et al., 2021 and Tchilibou et al., 2022). From these two main sites, IT spread over nearly 1000 km, and dissipate their energy. The model's depth-integrated internal tides energy dissipation (D_{bc}) is at least two times weaker than barotropic energy dissipation, with a mean value of 0.1 W.m^{-2} (Fig.2f). Approximately 30% of IT energy is dissipated locally over generation sites (not shown), consistent with the findings of Tchilibou et al. (2022). The remaining portion is dissipated offshore along the propagation path. This offshore dissipation is more extended along path A, ~300 km from the slope, with two beams spaced by an average distance of 120–150 km corresponding to mode-1 wavelength. On the other hand, there is less offshore dissipation along path B, occurring around 100–200 km from the slope (Fig.2f).

Another important characteristic of IT is their SSH imprints along the propagation pathway. The estimate of this signature deduced from the altimeter tracks (Fig.2g) produced by Zaron (2019) is compared with our model (Fig.2h), with the shelf masked over 150 m depth. Our model shows good agreement with this product, albeit with a slight overestimation of about ~1.5 cm on the SSH maxima. It is worth noting that the model's baroclinic SSH is an average over the year 2015, while the satellite estimate is an average over a longer period of about 20 years. The longer period of the satellite estimate may introduce greater variability in the altimeter tracks, potentially reducing the amplitude of the estimates and explaining the slight differences with the model in the positioning and amplitude of the maxima.

III.2. Temperature validation

Figure 3 shows the mean SST over the entire 2013–2015 period for TMI (Fig.3a), the tidal simulations (Fig.3b) and the non-tidal simulations (Fig.3c). We obtain the bias between TMI SST and the two simulations by linear interpolation of the simulations data on the observation grid. The simulations with tides accurately reproduce the spatial distribution of the observations, as indicated by the weak bias ($< \pm0.1℃$) with TMI SST. This is particularly evident for the cooling on the shelf around 47.5°W and to the southeast between 40°W–35°W and 2°S–2°N (Fig.3d). In contrast, the non-tidal simulations exhibit a warm bias of about 0.3°C in this cooling region (Fig.3e). To the northeast, between 50°W–54°W and 3°N–8°N in the Amazon plume, the SST of the non-tidal simulations is in better agreement with the observations, while the SST of the tidal simulations is about 0.6 °C cooler than TMI SST (Fig.3d). This bias is consistent with other models that include tides in this northern zone (e.g., Hernandez et al., 2016, 2017; Gévaudan et al. (2022). Far offshore, between 50°W–40°W and

6°N–10°N, both simulations exhibit a negative bias of about 0.2–0.3 °C (Fig.3d–e). We averaged the observations and interpolated simulation data within the dashed box (Fig.3a–c), with a depth of less than 200 m masked. This location of the boxes comprises IT generation sites and part of their pathways. We then computed the seasonal cycle of the three products (Fig.3f). The tidal and non-tidal simulations accurately reproduce both the seasonal cycle and the standard deviation of the observations, with low root mean square errors of approximately $2 \times 10^{-2} °C$ and $4 \times 10^{-2} °C$, respectively, when compared to the TMI SST. This indicates the robustness of the model's simulations. Over the seasonal cycle, the tidal simulations are closer to the observations from January to March, July to September, and November to December. During the rest of the year, either both simulations are equally close to the observations, or the non-tidal simulations are closer.

To gain insight into our model performance along the depth, we used the mean WOA2018 climatology (2005–2017) and simulation data (salinity and temperature) for the three years 2013–2015, averaged in the same region as in Fig.3f. Figure 3g shows the Temperature-Salinity (T-S) diagram for WOA2018 and the two simulations. The data are averaged in the box as before, and we use σ_θ [ρ-1000] to represent the density contours, with ρ the water density. Both simulations exhibit similar patterns as WOA2018 for deeper waters, i.e., T < 17 °C and σ_θ > 25.6 kg.m^{-3}. However, there exist minor discrepancies for the surface layer waters, i.e., T > 17 °C and 22.4 > σ_θ < 25.6 kg.m^{-3}. At that level, the tidal simulations better reproduce the T-S profile of the observations. These slight differences between WOA2018 observations and the two simulations, especially with the tidal simulations, further demonstrate the ability of our model to reproduce the observed water mass properties.

IV. Results

In this section, we present the influence of tides on temperature, the associated processes, and the impact on the atmosphere-ocean net heat exchange. The analyses were performed on a seasonal scale between April-May-June (AMJ) and August-September-October (ASO) for the three years 2013–2015.

IV.1. Tide-enhanced surface cooling

During the first season, warm waters, which are defined as > 27.6°C, dominate near the coast, especially in the middle shelf and in the south-east, and cold waters are present offshore north of 6°N (Fig.4a–c). Off the mouth of the Amazon River, water colder than 28.2 °C spreads between 43°W–51°W for TMI SST (Fig.4a) and tidal simulations (Fig.4b), while warmer

319 waters are present in the same area for the simulations without tides (Fig.4c). Figures 4d–f show

320 the SST, averaged over the ASO season. TMI SST (Fig.4d) shows an upwelling cell represented

321 by the extension of the 27.2 °C isotherm (white dashed contour) along the slope to about 49°W–

322 3°N towards the north-east of the region, which forms the extension of the ACT. This extension

323 also exists in the tidal simulations (Fig.4e), whereas $\leq$ 27.2 °C waters are not crossing 45.5°W

324 and remain in the southern hemisphere in the simulations without tides (Fig.4f). This means

325 that waters colder than 27.2°C can only extend further into the northeast because of tides. In

326 addition, we can note that the mean SST shows a very contrasting distribution between the two

327 seasons. There are warm waters along the shelf and cold waters offshore during the AMJ season

328 (Fig.4a-c). This is followed by warming along the Amazon plume and offshore, and an

329 upwelling cell in the south-east (Fig.4d-f).

330   The general impact of the tides, illustrated by the SST anomaly between the tidal and

331 the non-tidal simulations, is a cooling over a large part of the study area with maxima up to 0.3

332 °C (Fig. 5a–b). For ASO, tides induce a warming (> 0.3 °C) on the shelf at the mouth of the

333 Amazon River (Fig.5b), while for AMJ it is a cooling of the same intensity (Fig.5a). That

334 difference will be further discussed. Out of the shelf, the structure of temperature anomaly

335 varies depending on the season, probably because of seasonal mesoscale variability.

IV.2. Impact of the tides on the atmosphere-ocean net heat flux

337   The atmosphere-ocean net heat flux (Qt) reflects the balance of incoming and outgoing

338 heat fluxes across the atmosphere-ocean interface (see details on Moisan and Niiler, 1998;

339 Jayakrishnan and Babu, 2013). During AMJ, tides mainly induce positive Qt anomalies over

340 the whole domain. The average values are around 25 W.m^{-2} in the plume and the Amazon

341 retroflection to the northeast and along A and B (Fig.5c). Negative SST anomalies (~0.3°C)

342 occur throughout the domain in the same location. During the ASO season, at the mouth of the

343 Amazon, there are negative Qt anomalies but of the same magnitude as during the previous

344 season (Fig.5d). At this location, positive temperature anomalies (~0.3°C) are observed

345 (Fig.5b). Elsewhere, there are positive Qt anomalies and negative SST anomalies. It therefore

346 appears that negative SST anomalies induce positive Qt anomalies and vice versa. Hence, the

347 spatial structures of Qt anomalies and SST anomalies fit together for the two seasons. There is

348 a strong negative correlation of 0.97 with a significance of $R^2 = 0.95$ for the AMJ season, and

349 almost the same in ASO season with 0.98 and 0.96, respectively for the correlation and its

350 significance (Fig.5e). This is consistent with the fact that the atmosphere and the underlying

351 ocean are balanced. Then, the SST cooling induced by upwelled cold water will try upset this

balance. As a result of this, an equivalent variation in the net heat flux from the atmosphere to the ocean will attempt to restore it.

Figure 5f the integral over the entire domain of the net heat flux for each season and for each simulation. During the AMJ season, Qt increases from 23.85 TW (1 TW = 10^{12} W) for the non-tidal simulations to 35.7 TW for the tidal simulations, i.e., an increase of 33.2 %. That is, the tides are responsible for a third of Qt variation. This is very large compared to what is observed elsewhere in other IT hotspots (e.g., 15% in Solomon Sea, Tchilibou et al., 2020). During the second season, there is a smaller increase in Qt of about 7.4% between the two simulations, i.e., from 73.03 TW to 78.83 TW for the non-tidal and tidal simulations respectively (Fig.5f).

It is also worth noting the significant difference in integrated Qt between the two seasons. The values are less than 36 TW during the AMJ season, whereas they are around twice as high, > 73 TW, during the ASO season. Given that colder SST induce a stronger Qt, these higher values are likely related to the arrival of cold waters from ACT, which forms upwelling cells (Fig.4d–f) with a secondary tidal effect.

IV.3. Vertical structure of Temperature along internal tides pathway

To further analyze the temperature changes between the two simulations, we made vertical sections following the path of IT radiating from sites A and B (respectively black and red line in Fig.2f). Hereunder, only the transects following the pathway A are presented, since the vertical structure is similar following pathway B especially for AMJ season and because some processes tend to be null along pathway B during the ASO season. The mixed layer refers to a quasi-homogenous surface layer of temperature-dependent density that interacts with the atmosphere (Kara et al., 2003). Its maximum depth, also known as mixed-layer depth (MLD), is defined as the depth where the density increases from the surface value, due to temperature change of $|\Delta T| = 0.2\ °C$ with constant salinity (e.g., Dong et al., 2008; Varona et al., 2019).

Figure 6 shows the vertical sections of temperature for the two seasons following A. In AMJ season, over the slope and near the coast, cold waters (< 27.6 °C) remain below the surface at ~20 m for the tidal simulations (Fig.6a) and deeper at ~60 m for the non-tidal simulations (not shown). The cold waters rise to the surface more than 400 km offshore for both simulations. In surface layers (< 40 m), the temperature anomaly is more than -0.8°C at the shelf beak and less than -0.2°C elsewhere (Fig.6b). Further down (< 60m) the water column, this anomaly becomes much larger along the transect. Above that thermocline (< 120 m), the simulations with tides are colder by 1.2 °C from the slope, where IT are generated and following their

propagation pathway. Conversely, below the thermocline, the tidal simulations are warmer by the same intensity along the propagation path and down to ~300 m depth (Fig.6b). In AMJ season, the thermocline depth is about 100±15 m and MLD is about 40±20 m (Fig.6a). They both have a very weak slope between the coast and the open ocean. Over the whole domain, the thermocline is deeper by about 15 m on average in the non-tidal simulations, following the propagation paths of internal tides, on the Amazon shelf and plume (Fig.6c). Similarly, the MLD in the non-tidal simulations is deeper by approximately 10 m over the shelf, ~4 m along IT propagation paths and close to zero in the Amazon plume (Fig.6d).

In ASO season, cold waters previously confined below the surface during the previous season (AMJ) rise to the surface. These cold waters extend over the slope and up to about 150 km offshore in the non-tidal simulations (not shown) and up to 250 km offshore in the tidal simulations (Fig.7a). The 27.2 °C isotherm only reaches the surface above the slope in the tidal simulations and remains below the surface (~30 m) in the non-tidal simulations (not shown). This aligns with the absence of that isotherm at this location in the corresponding SST map (Fig.4f). For the tidal simulations, the temperature anomaly in the ASO season is smaller (~ -0.4 °C, Fig.7b) in the surface layers (< 40 m) near the coast compared to the AMJ season (Fig.6b). In contrast, during the ASO season, this cooling can drive more SST anomalies along A (-0.3 °C, Fig.5b). A stronger cooling of about 1.2 °C occurs deeper between 60 and 140 m depth, and a warming of about 1.2 °C below, which extends less offshore than during AMJ season, 650 km vs. ~1000 km. In ASO season, the coastward slope of the thermocline and MLD becomes steeper compared to AMJ season. In both simulations, there is a dip of ~80 m, i.e., ~60 m offshore and ~140 m inshore, for the thermocline (Fig.7a), and a dip of ~40 m, i.e., ~30 m offshore and ~70 m inshore, for MLD (Fig.7a). Over the entire domain, tides reduce the thermocline depth by ~6 m on the shelf and ~12 m at the plume and far offshore along the propagation path of A (Fig.7c), and they MLD by about 10 m along the shelf and ~4 m along the propagation path of A (Fig.7d).

Between the two seasons, there is also a change in the vertical density gradient between the coast and the open sea. In tidal simulations, during AMJ season, the isopycnals layers are thin near the coast and thicken towards the open sea (Fig.6a). This means that a strong stratification is present near the coast and decreases towards the open sea. In contrast, during ASO season, the isopycnals layers are thicker near the coast and tight offshore (Fig.7a). As the result of this, the stratification is weaker inshore than offshore. This clearly highlights a seasonality in the vertical density gradient profile in agreement with Tchilibou et al. (2022).

418   Note that this behavior also appears in the simulations without tides (not shown). The transects

419   of the temperature anomaly show that tides influence the temperature in the ocean from the

420   surface to the deep layers, with a greater effect on the first three hundred meters. One question

421   we address in this paper is to better understand what processes are at work that explain these

422   temperature changes.

IV.4. What are the processes involved?

424   To explain the observed surface and water column temperature changes, we computed

425   and analyzed the terms of the heat balance equation (see Section II.3.2, Equation 6) for both

426   seasons (AMJ and ASO).

IV.4.1. Vertical diffusion of Temperature

428   Figure 8 shows the vertical temperature diffusion tendency (ZDF). ZDF is averaged

429   between 2–20 m, i.e., within the mixed layer. For the AMJ season, ZDF in the tidal simulations

430   (Fig.8a) shows a negative trend (i.e., cooling) in the whole domain. The maximum values ($>$

431   $|0.4|$°C.day^{-1}) are located along the slope where IT are generated and on their propagation

432   path. There is a larger horizontal extent along A of ~700 km from the coasts compared to B,

433   where it is ~300 km from the coasts. Elsewhere, ZDF is weak ($>$ -0.1 °C.day^{-1}). For the non-

434   tidal simulations (Fig.8b), ZDF is weak over the entire domain ($>$ -0.1 °C.day^{-1}). In ASO

435   season, the tidal simulations (Fig.8c) show a decrease of the ZDF near the coast ($<$ 100 km) and

436   a strengthening offshore along A compared to the previous season, but with the same cooling

437   trend ($<$ -0.4 °C.day^{-1}). Along B, it tends to be null, both at the coast and offshore (Fig.8c). In

438   addition, the mesoscale circulation and eddy activity intensify during this season. To the

439   northeast, between 4°N–8°N, and 47°W–53°W, there is a cooling on the shelf of ~0.3 °C.day^{-1}

440   with eddy-like patterns in the tidal simulations (Fig.8c). The processes by which these features

441   might arise are discussed in more details in Section V. Unsurprisingly, ZDF is weak everywhere

442   for the non-tidal simulations (Fig.8d). IT are the dominant driver of vertical diffusion of

443   temperature along the shelf break and offshore, while the mixing induced by barotropic tides

444   prevail on the shelf.

445   On the vertical following A, there are opposite sign ZDF values, with mean magnitude

446   of ~ $|0.4|$ °C.day^{-1}. These values are centered around the thermocline for the simulations with

447   tides in the two seasons AMJ and ASO (respectively Fig.8e and 8f). There is a cooling trend

448   above the thermocline and a warming trend below. The average vertical extent is up to ~350 m

449   depth for the maximum values but exceeds 500 m depth for the low values ($<$ 0.1 °C.day^{-1}).

450 As for the horizontal averages (Fig.8a and 8c), from one season to another there is a weakening

451 of ZDF above the slope and a strengthening offshore, Fig.8e and 8f, for AMJ and ASO,

452 respectively. Furthermore, offshore ZDF maxima are discontinuous and spaced of about 140–

453 160 km during the AMJ season (Fig.8e) but are more continuous for the ASO season (Fig.8f).

454 For the non-tidal simulations, the mean ZDF tends to be null in the ocean interior but remains

455 quite large (> -0.2 °C.day^{-1}) in the thin surface layer during the two seasons (Fig.8g–h).

456   Furthermore, it is worth to noting that along IT propagation's pathway, the maximum

457 of the ZDF follows the maxima of the baroclinic tidal energy dissipation (Fig.2f). This proves

458 that the dissipation of IT causes vertical mixing that enhances SST cooling. In addition, this

459 temperature diffusion contributes to greater subsurface cooling within the mixed layer and

460 warming in the deeper layers beneath the thermocline.

461   The seasonality of the stratification, highlighted above, could explain why the ZDF is

462 stronger along the slope and the near-coastal pathway B during the AMJ season (Fig.8a and

463 8e), and why in ASO season ZDF is weaker along the slope, close to zero following B, and

464 reinforce offshore of A (Fig.8c and 8f). Previous studies have shown that stratification

465 influences the generation of internal tides and controls their modal distribution. Here we show

466 that stratification also plays a role on the fate of these internal tides, in this case on their

467 dissipation. The stratification could determine where IT dissipate their energy in the water

468 column, as mentioned by de Lavergne et al. (2020).

IV.4.2. Advection of temperature

470   The vertical (z–ADV) and the horizontal (h–ADV) terms of the temperature advection

471 tendency are averaged in the same depth-range as above for the two seasons.

IV.4.2.a Vertical advection of Temperature

473   Tides fail to generate vertical temperature advection within surface layers. As expected,

474 z–ADV is almost null throughout the region in that depth-range (Fig.9a–d). Nevertheless, for

475 both seasons, there are extreme values located in the northwest on the plateau between 54°W–

476 50°W and 3°N–6°N with the same intensity in the two simulations (<0.3 °C.day^{-1}). But deeper,

477 vertical sections (Fig.9a–h) show an intensification of z–ADV of about ±0.8 °C.day^{-1} located

478 below the MLD and seems to be centered around the thermocline, with a vertical extension

479 from 20–200 m depth. z–ADV is stronger in tidal simulations during both seasons (Fig.9e–f)

480 and presents sparse extrema offshore (>300 km) for the non-tidal simulations (Fig.9g–h). For

481 the simulations with tides, z–ADV appears to be dominated by a cooling trend, with a marked

hotspot on the slope followed by other hotspots offshore. These extreme values are spaced about 120–150 km apart, i.e., a mode-1 wavelength as for the baroclinic tidal energy dissipation (Fig.2f). Note that for both simulations (Fig.9e–h), the extreme values are located within the narrow density (σ_θ) contours [23.8–26.2 kg.m^{-3}], i.e., within the pycnocline. The location of the extreme values of z–ADV at the shelf break and along IT propagation pathways and its negative sign suggest that the diffusive part of the advection scheme may account significantly in z–ADV.

IV.4.2.b Horizontal advection of temperature

Horizontal advection of temperature (h–ADV) is defined as the sum of the zonal (x–ADV) and meridional (y–ADV) terms of temperature advection tendency. As for z–ADV, the mean of h–ADV tends to be null over the entire domain in the surface layers for both seasons in both simulations (Fig.10a–d). Nevertheless, weak extremums exist in the northwest of the plateau between 54°W–50°W and 3°N–7°N. These intensify during the ASO season in both simulations, ∼ ±0.2 °C.day^{-1}, Figure 10c and 10d for the tidal and non-tidal simulations, respectively. In AMJ season, h–ADV is slightly stronger, ∼0.1 °C.day^{-1}, around sites A and B in the tidal simulations (Fig.10a), which appears to be related to IT generated along the slope. However, there is a slight distinction between the two simulations in the surface layers, suggesting that tides have a minimal effect on h–ADV, as expected. Consequently, h–ADV has a negligible influence on the cold-water tongue observed in the surface SST during the ASO season (Fig.4d–f).

Along the vertical following A, h–ADV maxima are confined below the mixed-layer depth. The tidal simulations (Fig.10e–f) exhibit significantly more intense values compared to the non-tidal simulations (Fig.10g–h). h–ADV contributes to both warming and cooling of the temperature, with a magnitude of about ±0.4 °C.day^{-1}, extending from the slope to over 500 km offshore. In both seasons, the average vertical extension lies between the surface and 400 m depth for the tidal simulations, and between 20–300 m depth for the non-tidal simulations. Similarly to z–ADV, h–ADV is stronger within the pycnocline. In the tidal simulations, a warming effect is observed above the slope (0.4 °C.day^{-1}), reaching the surface in both seasons. This vertical excursion is also observed for ZDF and z–ADV, and it is a marker of local dissipation of IT at their generation sites. It is noteworthy that the location of h–ADV maxima does not coincide with the dissipation hotspots of IT, in contrast of ZDF and z–ADV.

IV.4.3. Heat budget balance

From the sections above, it is evident that IT-induced mixing within the mixed layer emerges as the primary driver among the ocean's internal processes in explaining changes in SST. However, below MLD, advective processes play a more significant role in structuring temperature. Figure 10 presents the average of the terms of the Equation 6 below MLD within the depth range of 60–400 m. The analysis focuses on a specific region with latitude and longitude ranging between 0°N–6°N and 40°W–48°W, respectively. This region includes the two main IT paths, as well as a portion of the along-coast upwelling region. During the AMJ season, ADV is the dominant process over diffusion terms in both tidal (Fig.11a) and non-tidal (Fig.11b) simulations. However, in the ASO season, ADV only dominate in tidal simulations (Fig.11c), while ZDF dominates in non-tidal simulations (Fig.11d).

It therefore appears that ADV only have a considerable influence on temperature below MLD, contrasting with the study of Neto and da Silva (2014), which identify ADV as the primary driver causing along-coast SST cooling. However, we can assume that advection and mixing are interconnected. In other words, the water masses that are advected below MLD may undergo mixing within the surface layers due to the overall mixing occurring throughout the water column. Additionally, it is worth mentioning that in our simulations, *Asselin* has a negligible impact on temperature. Conversely, *Forcing* term does impact the temperature within the surface layers. However, we have not discussed this aspect in our analysis as our primary focus was on understanding the internal processes of the ocean.

V. Discussion

V.1. The mode-1 wavelength in the vertical terms of the heat budget equation

Along the vertical and towards the open ocean, both ZDF and z-ADV exhibit a wave-like structure, with patches that are spaced apart by about 120–160 km typical of mode-1 wavelength. However, during the ASO season, this pattern is not observed for ZDF. Instead, ZDF values appear more continuous along the transect, likely due to additional mixing caused by the breaking of incoherent IT that intensify during that season. Furthermore, de Macedo et al. (2023) recently provided a detailed description of internal solitary waves (ISW) in the same region based on remote sensing data. These ISWs originate from instabilities and energy loss or dissipation of IT radiating from the slope, primarily along pathways A and B (Magalhaes et al., 2016). The first study demonstrated that the inter-packet distance of ISWs corresponds to the mode-1 wavelength. Interestingly, the positions of IT dissipation hotspots, as well as z–

545 ADV patches in both seasons and ZDF patches, especially during the AMJ season, in our model

546 align with the observed occurrences of ISWs (refer to Figure 2 in their study). This provides

547 evidence that our model accurately reproduces the location of IT dissipation.

V.2. Temperature changes over the shelf: two main competitive processes

549 In the simulation without tides, there is a strong along-coast current exiting northwesterly

550 the mouth of the Amazon River (e.g., Ruault et al., 2020) with an average intensity lower

551 than 0.5 m.s^{-1} in the first 50 meters for both seasons (Fig.12a–b). When including tides in the

552 model, the latter study showed that there is an increase in the vertical mixing in the water

553 column due to stratified-shear flow instability, which weakens and deflects the along-coast

554 current north-eastwards at the mouth of the Amazon River (Fig.12c–d) and favors cross-shore

555 export of water. We can therefore establish that there are at least two processes at work: (i)

556 vertical mixing and (ii) horizontal transport, backed respectively by ZDF and h–ADV. We then

557 looked at the latter two processes along the vertical following the cross-shore transect (*C-S*)

558 defined in Figure 10c. Hereinafter, "inner mouth" refers to the part of the transect within 200

559 km from the shore, whereas "outer shelf" refers to the part beyond.

560 During the AMJ season, in the inner mouth of the region, the flow of the river becomes

561 dominant. The tide-induced vertical mixing in the narrow water column results in the warming

562 and deepening of the thermocline (Fig.13a–b). Conversely, on the outer shelf, this mixing

563 occurs in a thicker water column, leading to cooling above the thermocline and warming below

564 (Fig.13a). This pattern extends across the shelf and along the pathways of internal tides, as

565 shown in Section IV.4.1 (refer to Fig.8a and 8e). In this season, the weaker circulation may

566 result in low values of h–ADV (Fig.13b). Therefore, during the first season, the dominant

567 process that explains the average negative SST anomaly over the shelf appears to be vertical

568 mixing.

569 During the second season, there is a significant increase in solar radiation on the shelf, with

570 an average value of 60 W.m^{-2}, compared to the previous season (Fig.13c). Additionally, the

571 average depth of the thermocline deepened further offshore (Fig.13d and 13e). In this season,

572 mixing processes lead to warming in the thin surface layer, specifically in depths less than 2m

573 (Fig.13d). NBC is stronger, resulting in an increase of the transport over the shelf (Prestes et

574 al., 2018). It is also important to consider the small mean tidal residual transport (Bessières et

575 al., 2008), which reinforces the stronger current transport. These factors contribute to a more

576 dynamic region and an increase in h–ADV (Fig.13e). Consequently, h–ADV plays a significant

role in determining SST on the shelf. For this season, the combination of these two processes explains the observed positive SST anomaly.

Additionally, from the AMJ to ASO seasons, there is a notable deepening of the thermocline depth on the outer shelf. This observation has previously been highlighted by Silva et al. (2005) from REVIZEE (Recursos Vivos da Zona Econômica Exclusiva) campaign data, further validating of our simulations.

V.3. Mixing in the NBC retroflection area

To the north-west of the domain [3°N–9°N and 53°W–45°W], in the surface layers (2–20m), eddy-like or circular patterns exist in ZDF during the ASO season for the simulation including tides (Fig.8c). NBC intensifies and retroflects, and strong eddy activity takes place there during ASO. We can assume that this intense mesoscale activity influences the mixing and subsequent temperature diffusion. However, it is not yet clear how these mesoscale features produce mixing. Fronts exist in such region and are associated with high horizontal temperature gradient (∇T) and significant vertical mixing (see Chapman et al., 2020). We therefore examined the mean ∇T in the same depth range as ZDF (2–20 m). During the AMJ season, ∇T is on average equal to 4×10^{-2} °C/10 km. As expected, it does not reveal any circular fronts for the two simulations since mesoscale activity is low (Fig.14a–b). ∇T increases in ASO season [$> 5 \times 10^{-2}$ °C/10 km] in the north-west and exhibits circular and filamentary fronts in both simulations (Fig.14c–d). Therefore, one would expect to see the same circular patterns in ZDF for both simulations, this is not actually the case (see Fig.8c–d). Another hypothesis is that these circular patterns could be originated from the interaction between IT and near-inertial oscillations, which can enhance mixing and vertical transport processes in the ocean. But quantifying this interaction requires further analysis and is beyond the scope of this study.

VI.   Summary

This paper investigates the influence of internal tidal (IT) on temperature and associated processes through twin simulations including or excluding tidal forcing, using the NEMO model configuration called AMAZON36. Our tidal simulations accurately reproduce the generation and dissipation of IT. When comparing the simulations including tides to observations, there is a better agreement in sea surface temperature (SST) and water mass properties along the vertical. We then focus our analysis on a three-year period (2013–2015) and two seasons, AMJ and ASO, which have contrasting stratification, circulation and IT activity.

609   Results demonstrate that tides cause a cooling effect in SST of 0.3°C in the Amazon
610 offshore plume and along the paths of IT in both seasons. In the ASO season particularly, tides
611 enhance seasonal upwelling, leading to cooler SST. Over the Amazon shelf, tides induce
612 cooling in AMJ and warming in ASO. These cooling/warming patterns over the region affect
613 the net heat flux between the atmosphere and the ocean (Qt). As the result, there is an overall
614 increase of Qt from 33.2% in AMJ to 7.4% in ASO. Changes in Qt in such large atmospheric
615 convection regions can reduce cloud convection into the atmosphere (Koch-Larrouy et al.,
616 2010). Therefore, understanding changes in tidal activity become crucial to better assess climate
617 change (Yadidya and Rao, 2022).

618   In the subsurface in both seasons, the findings reveal that tides induce stronger cooling
619 above the thermocline (<120m) and warming below (> 120–300m), with a mean magnitude of
620 about 1.2°C.

621   The analysis of the heat budget equation reveals that within the mixed layer, the
622 temperature changes are primarily influenced by the vertical diffusion of temperature (ZDF).
623 This diffusion is driven by diapycnal mixing, which results from barotropic tide bottom friction
624 over the shallow shelf and the breaking of IT at their generation sites and along their
625 propagation pathways. It is noteworthy that the ZDF values are highest in these latter two areas.
626 In deeper layers below the mixed layer, ZDF combines with vertical and horizontal advection
627 terms (z–ADV and h–ADV) to explain temperature changes. Notably, ZDF and z–ADV patches
628 coincide with dissipation hotspots of IT energy.

629   This study highlights the importance of the intensified mixing of IT for temperature
630 structure. We focused hereabove on describing the impacts of tides in temperature on a seasonal
631 scale. However, a companion paper will then analyze the variability of temperature at tidal and
632 subtidal scales using our simulations and remote sensing data.

633   Furthermore, other analysis from our simulations revealed a significant impact on
634 salinity. In addition, IT was reported to be a source of nutrient uptake and impact the spatial
635 distribution of phytoplankton and zooplankton, and therefore on the entire food chain (Sharples
636 et al., 2007, 2009; Xu et al., 2020). Ongoing investigations is conducted to assess the impacts
637 of tides on marine ecosystems using a combined approach including:

638   1- the new designed coupled physical/biogeochemistry simulations from NEMO/PISCES
639   called *AMAZON36-BIO* and;
640   2- *in situ* data, consisting of long-term PIRATA mooring data (Bourles et al., 2019) and
641   the recent Amazon mixing campaign (AMAZOMIX, Bertrand et al., 2021).

642

Data availability statements. The 2020 release of GEBCO bathymetry is publicly available online through: https://www.gebco.net/data_and_products/gridded_bathymetry_data/gebco_2020/. The TMI SST v7.1 data are publicly available online from the REMSS platform: https://www.remss.com/missions/tmi/, last access: 27 June 2022. WOA2018 climatology is publicly available online at: https://www.ncei.noaa.gov/access/world-ocean-atlas-2018/, last access: 27 June 2022. The model simulations are available upon request by contacting the corresponding author.

Authors contributions. AKL: Funding acquisition; FA, AKL, and ID: Conceptualization and methodology; GM and FA, with assistance from JC and AKL: Numerical simulations; Formal analysis: FA with interactions from all co-authors; Preparation of the manuscript; FA with contributions from all co-authors.

Competing interests. The authors declare that they have no conflict of interest.

Disclaimer. Publisher's note: Copernicus Publications remains neutral regarding jurisdictional claims in published maps and institutional affiliations.

Acknowledgements. The Authors would like to thank the Remote Sensing System (REMSS) for providing TMI SST datasets, and the NASA's National Center for Environmental Information (NCEI) for providing World Ocean Atlas 2018 (WOA2018) data. The Authors would like to thank the Editorial team for their availability and are grateful to the two Reviewers Clément Vic and Nicolas Grisouard for their valuable comments, which helped to improve the quality of the present work.

Funding. This work is part of the PhD Thesis of FA, cofounded by Institut de Recherche pour le Développement (IRD) and Mercator Ocean International (MOi), under the co-advising of AKL and ID. The numerical simulations were founded by CNES/CNRS/IRD via the projects A0080111357 and A0130111357 and were performed thank to "Jean-Zay", the CNRS/GENCI/IDRIS platform for modelling and computing.

672

673   *Review statement.* This paper was edited by Rob Hall and reviewed by Clément Vic and Nicolas

674   Grisouard.

675

676   **References**

677   Aguedjou, H.M.A., Chaigneau, A., Dadou, I., Morel, Y., Pegliasco, C., Da-Allada, C.Y.,
678   Baloïtcha, E.: What Can We Learn From Observed Temperature and Salinity Isopycnal
679   Anomalies at Eddy Generation Sites? Application in the Tropical Atlantic Ocean, J.
680   Geophys. Res. Oceans, 126, JC017630, https://doi.org/10.1029/2021JC017630, 2021.

681   Aguedjou, H.M.A., Dadou, I., Chaigneau, A., Morel, Y., Alory, G.: Eddies in the Tropical
682   Atlantic Ocean and Their Seasonal Variability, Geophys. Res. Lett., 46, 12156-12164,
683   https://doi.org/10.1029/2019GL083925, 2019.

684   Archer, D., Martin, P., Buffett, B., Brovkin, V., Rahmstorf, S., Ganopolski, A.; The importance
685   of ocean temperature to global biogeochemistry, Earth Planet. Sci. Lett., 222, 333-348,
686   https://doi.org/10.1016/j.epsl.2004.03.011, 2004.

687   Baines, P.G.: On internal tide generation models, Deep Sea Res. Part Oceanogr. Res. Pap., 29,
688   307-338, https://doi.org/10.1016/0198-0149(82)90098-X, 1982.

689   Barbot, S., Lyard, F., Tchilibou, M., Carrere, L.: Background stratification impacts on internal
690   tide generation and abyssal propagation in the western equatorial Atlantic and the Bay
691   of Biscay, Ocean Sci., 17, 1563-1583, https://doi.org/10.5194/os-17-1563-2021, 2021.

692   Barton, E.D., Inall, M.E., Sherwin, T.J., Torres, R.: Vertical structure, turbulent mixing and
693   fluxes during Lagrangian observations of an upwelling filament system off Northwest
694   Iberia, Prog. Oceanogr. Lagrangian studies of the Iberian upwelling system, 51, 249-
695   267, https://doi.org/10.1016/S0079-6611(01)00069-6, 2001.

696   Beardsley, R.C., Candela, J., Limeburner, R., Geyer, W.R., Lentz, S.J., Castro, B.M.,
697   Cacchione, D., Carneiro, N.: The M2 tide on the Amazon Shelf, J. Geophys. Res.
698   Oceans, 100, 2283-2319, https://doi.org/10.1029/94JC01688, 1995.

699   Bertrand, A., De Saint Leger, E., and Koch-Larrouy, A.: AMAZOMIX 2021, French
700   Oceanographic Cruises, https://doi.org/10.17600/18001364, 2021.

701   Bessières, L.: Impact des marées sur la circulation générale océanique dans une perspective
702   climatique, Ph.D Thesis, Océan Atmosphère, Université Paul Sabatier - Toulouse III,
703   France, 179pp., 2007.

704   Bessières, L., Madec, G., Lyard, F.: Global tidal residual mean circulation: Does it affect a
705   climate OGCM?, Geophys. Res. Lett., 35(3), L03609,
706   https://doi.org/10.1029/2007GL032644, 2008.

707   Bourles, B., Molinari, R.L., Johns, E., Wilson, W.D., Leaman, K.D.: Upper layer currents in
708   the western tropical North Atlantic (1989–1991), J. Geophys. Res. Oceans, 104, 1361-
709   1375, https://doi.org/10.1029/1998JC900025, 1999.

710   Bourles, B., Araujo, M., McPhaden, M.J., Brandt, P., Foltz, G.R., Lumpkin, R., Giordani, H.,
711   Hernandez, F., Lefèvre, N., Nobre, P., Campos, E., Saravanan, R., Trotte-Duhà, J.,
712   Dengler, M., Hahn, J., Hummels, R., Lübbecke, J.F., Rouault, M., Cotrim, L., Sutton,
713   A., Jochum, M., Perez, R.C.: PIRATA: A Sustained Observing System for Tropical
714   Atlantic Climate Research and Forecasting, Earth Space Sci., 6, 577-616,
715   https://doi.org/10.1029/2018EA000428, 2019.

716   Buijsman, M.C., Arbic, B.K., Richman, J.G., Shriver, J.F., Wallcraft, A.J., Zamudio, L.:
717   Semidiurnal internal tide incoherence in the equatorial Pacific, J. Geophys. Res. Oceans,
718   122, 5286-5305, https://doi.org/10.1002/2016JC012590, 2017.

Chapman, C.C., Lea, M.-A., Meyer, A., Sallée, J.-B., Hindell, M.: Defining Southern Ocean fronts and their influence on biological and physical processes in a changing climate, Nat. Clim. Change, 10, 209-219, https://doi.org/10.1038/s41558-020-0705-4, 2020.

Clayson, C.A., Bogdanoff, A.S.: The Effect of Diurnal Sea Surface Temperature Warming on Climatological Air–Sea Fluxes, Am. Meteorol. Soc., 26, 2546-2556, https://doi.org/10.1175/JCLI-D-12-00062.1, 2013.

Collins, M., An, S.-I., Cai, W., Ganachaud, A., Guilyardi, E., Jin, F.-F., Jochum, M., Lengaigne, M., Power, S., Timmermann, A., Vecchi, G., Wittenberg, A.: The impact of global warming on the tropical Pacific Ocean and El Niño, Nat. Geosci., 3, 391-397, https://doi.org/10.1038/ngeo868, 2010.

de Lavergne, C., Vic, C., Madec, G., Roquet, F., Waterhouse, A.F., Whalen, C.B., Cuypers, Y., Bouruet-Aubertot, P., Ferron, B., Hibiya, T.: A Parameterization of Local and Remote Tidal Mixing, J. Adv. Model. Earth Syst., 12, MS002065, https://doi.org/10.1029/2020MS002065, 2020.

de Macedo, C. R., Koch-Larrouy, A., da Silva, J. C. B., Magalhães, J. M., Lentini, C. A. D., Tran, T. K., Rosa, M. C. B., and Vantrepotte, V.: Spatial and temporal variability in mode-1 and mode-2 internal solitary waves from MODIS-Terra sun glint off the Amazon shelf, Ocean Sci., 19, 1357–1374, https://doi.org/10.5194/os-19-1357-2023, 2023.

Didden, N., Schott, F.: Eddies in the North Brazil Current retroflection region observed by Geosat altimetry, J. Geophys. Res. Oceans, 98, 20121-20131, https://doi.org/10.1029/93JC01184, 1993.

Dong, S., Sprintall, J., Gille, S.T., Talley, L.: Southern Ocean mixed-layer depth from Argo float profiles, J. Geophys. Res. Oceans, 113, C06013, https://doi.org/10.1029/2006JC004051, 2008.

Dunphy, M., Lamb, K.G.: Focusing and vertical mode scattering of the first mode internal tide by mesoscale eddy interaction, J. Geophys. Res. Oceans, 119, 523-536, https://doi.org/10.1002/2013JC009293, 2014.

Egbert, G.D., Ray, R.D.: Significant dissipation of tidal energy in the deep ocean inferred from satellite altimeter data, Nature, 405, 775-778, https://doi.org/10.1038/35015531, 2000.

Fassoni-Andrade, A.C., Durand, F., Azevedo, A., Bertin, X., Santos, L.G., Khan, J.U., Testut, L., Moreira, D.M.: Seasonal to interannual variability of the tide in the Amazon estuary, Cont. Shelf Res., 255, 104945, https://doi.org/10.1016/j.csr.2023.104945, 2023.

Fontes, R.F.C., Castro, B.M., Beardsley, R.C.: Numerical study of circulation on the inner Amazon Shelf, Ocean Dyn., 58, 187-198, https://doi.org/10.1007/s10236-008-0139-4, 2008.

Gabioux, M., Vinzon, S.B., Paiva, A.M.: Tidal propagation over fluid mud layers on the Amazon shelf, Cont. Shelf Res., 25, 113-125, https://doi.org/10.1016/j.csr.2004.09.001, 2005.

Garzoli, S.L., Ffield, A., Yao, Q.: North Brazil Current rings and the variability in the latitude of retroflection, Elsevier Oceanography Series, 68, 357-373, https://doi.org/10.1016/S0422-9894(03)80154-X, 2003.

Gévaudan, M., Durand, F., Jouanno, J.: Influence of the Amazon-Orinoco Discharge Interannual Variability on the Western Tropical Atlantic Salinity and Temperature, J. Geophys. Res. Oceans, 127, JC018495, https://doi.org/10.1029/2022JC018495, 2022.

Hernandez, O., Jouanno, J., Durand, F.: Do the Amazon and Orinoco freshwater plumes really matter for hurricane-induced ocean surface cooling?, J. Geophys. Res. Oceans, 121, 2119-2141, https://doi.org/10.1002/2015JC011021, 2016.

Hernandez, O., Jouanno, J., Echevin, V., Aumont, O.: Modification of sea surface temperature by chlorophyll concentration in the Atlantic upwelling systems, J. Geophys. Res. Oceans, 122, 5367-5389, https://doi.org/10.1002/2016JC012330, 2017.

Hersbach, H., Bell, B., Berrisford, P., Hirahara, S., Horányi, A., Muñoz-Sabater, J., Nicolas, J., Peubey, C., Radu, R., Schepers, D., Simmons, A., Soci, C., Abdalla, S., Abellan, X., Balsamo, G., Bechtold, P., Biavati, G., Bidlot, J., Bonavita, M., De Chiara, G., Dahlgren, P., Dee, D., Diamantakis, M., Dragani, R., Flemming, J., Forbes, R., Fuentes, M., Geer, A., Haimberger, L., Healy, S., Hogan, R.J., Hólm, E., Janisková, M., Keeley, S., Laloyaux, P., Lopez, P., Lupu, C., Radnoti, G., de Rosnay, P., Rozum, I., Vamborg, F., Villaume, S., Thépaut, J.-N.: The ERA5 global reanalysis, Q. J. R. Meteorol. Soc., 146, 1999-2049, https://doi.org/10.1002/qj.3803, 2020.

Jayakrishnan, P.R., Babu, C.A.: Study of the Oceanic Heat Budget Components over the Arabian Sea during the Formation and Evolution of Super Cyclone Gonu, Atmospheric and Climate Sciences, 3, 282-290, https://doi.org/10.4236/acs.2013.33030, 2013.

Jithin, A.K., Francis, P.A.: Role of internal tide mixing in keeping the deep Andaman Sea warmer than the Bay of Bengal, Scientific Reports, 10, 11982, https://doi.org/10.1038/s41598-020-68708-6, 2020.

Johns, W.E., Lee, T.N., Schott, F.A., Zantopp, R.J., Evans, R.H.: The North Brazil Current retroflection: Seasonal structure and eddy variability, J. Geophys. Res. Oceans, 95, 22103-22120, https://doi.org/10.1029/JC095iC12p22103, 1990.

Johns, W.E., Lee, T.N., Beardsley, R.C., Candela, J., Limeburner, R., Castro, B.: Annual Cycle and Variability of the North Brazil Current, J. Phys. Oceanogr., 28, 103-128, https://doi.org/10.1175/1520-0485(1998)028<0103:ACAVOT>2.0.CO;2, 1998.

Jouanno, J., Marin, F., du Penhoat, Y., Sheinbaum, J., Molines, J.-M.: Seasonal heat balance in the upper 100 m of the equatorial Atlantic Ocean, J. Geophys. Res. Oceans, 116, C09003, https://doi.org/10.1029/2010JC006912, 2011.

Kara, A.B., Rochford, P.A., Hurlburt, H.E.: Mixed layer depth variability over the global ocean, J. Geophys. Res. Oceans, 108(C3), 3079, https://doi.org/10.1029/2000JC000736, 2003.

Kelly, S.M., Nash, J.D., Kunze, E.: Internal-tide energy over topography, J. Geophys. Res. Oceans, 115, C06014, https://doi.org/10.1029/2009JC005618, 2010.

Koch-Larrouy, A., Madec, G., Bouruet-Aubertot, P., Gerkema, T., Bessières, L., Molcard, R.: On the transformation of Pacific Water into Indonesian Throughflow Water by internal tidal mixing, Geophys. Res. Lett., 34, L04604, https://doi.org/10.1029/2006GL028405, 2007.

Koch-Larrouy, A., Madec, G., Iudicone, D., Atmadipoera, A., Molcard, R.: Physical processes contributing to the water mass transformation of the Indonesian Throughflow, Ocean Dyn., 58, 275-288, https://doi.org/10.1007/s10236-008-0154-5, 2008.

Koch-Larrouy, A., Lengaigne, M., Terray, P., Madec, G., Masson, S.: Tidal mixing in the Indonesian Seas and its effect on the tropical climate system, Clim. Dyn., 34, 891-904, https://doi.org/10.1007/s00382-009-0642-4, 2010.

Koch-Larrouy, A., Atmadipoera, A., van Beek, P., Madec, G., Aucan, J., Lyard, F., Grelet, J., Souhaut, M.: Estimates of tidal mixing in the Indonesian archipelago from multidisciplinary INDOMIX in-situ data, Deep Sea Res. Part Oceanogr. Res. Pap., 106, 136-153, https://doi.org/10.1016/j.dsr.2015.09.007, 2015.

Kosuth, P., Callède, J., Laraque, A., Filizola, N., Guyot, J.L., Seyler, P., Fritsch, J.M., Guimarães, V.: Sea-tide effects on flows in the lower reaches of the Amazon River, Hydrol. Process, 23, 3141-3150, https://doi.org/10.1002/hyp.7387, 2009.

Kunze, E., MacKay, C., McPhee-Shaw, E.E., Morrice, K., Girton, J.B., Terker, S.R.: Turbulent Mixing and Exchange with Interior Waters on Sloping Boundaries, J. Phys. Oceanogr., 42, 910-927, https://doi.org/10.1175/JPO-D-11-075.1, 2012.

817 Lambeck, K., Runcorn, S.K.: Tidal dissipation in the oceans: astronomical, geophysical and
818   oceanographic consequences, Philos. Trans. R. Soc. Lond. Ser. Math. Phys. Sci., 287,
819   545-594, https://doi.org/10.1098/rsta.1977.0159, 1977.

820 Lascaratos, A.: Estimation of deep and intermediate water mass formation rates in the
821   Mediterranean Sea, Deep Sea Res. Part II Top. Stud. Oceanogr., 40, 1327-1332,
822   https://doi.org/10.1016/0967-0645(93)90072-U, 1993.

823 Laurent, L.S., Garrett, C.: The Role of Internal Tides in Mixing the Deep Ocean, J. Phys.
824   Oceanogr., 32, 2882-2899, https://doi.org/10.1175/1520-
825   0485(2002)032<2882:TROITI>2.0.CO;2, 2002.

826 Le Provost, C., Florent, L.: Energetics of the M2 barotropic ocean tides: an estimate of bottom
827   friction dissipation from a hydrodynamic model, Science Direct Prog. Oceanogr., 40(1-
828   4), 37-52, https://doi.org/10.1016/S0079-6611(97)00022-0, 1997.

829 Leclair, M., Madec, G.: A conservative leapfrog time stepping method, Ocean Model, 30, 88-
830   94, https://doi.org/10.1016/j.ocemod.2009.06.006, 2009.

831 Lellouche, J.-M., Greiner, E., Le Galloudec, O., Garric, G., Regnier, C., Drevillon, M.,
832   Benkiran, M., Testut, C.-E., Bourdalle-Badie, R., Gasparin, F., Hernandez, O., Levier,
833   B., Drillet, Y., Remy, E., Le Traon, P.-Y.: Recent updates to the Copernicus Marine
834   Service global ocean monitoring and forecasting real-time 1∕12° high-resolution system,
835   Ocean Sci., 14, 1093-1126, https://doi.org/10.5194/os-14-1093-2018, 2018.

836 Lentini, C.A.D., Magalhães, J.M., da Silva, J.C.B., Lorenzzetti, J.A.: Transcritical Flow and
837   Generation of Internal Solitary Waves off the Amazon River: Synthetic Aperture Radar
838   Observations and Interpretation, Oceanography, 29(4), 187-195,
839   http://www.jstor.org/stable/24862294, 2016.

840 Lentz, S.J., Limeburner, R.: The Amazon River Plume during AMASSEDS: Spatial
841   characteristics and salinity variability, J. Geophys. Res. Oceans, 100, 2355-2375,
842   https://doi.org/10.1029/94JC01411, 1995.

843 Li, C., Zhou, W., Jia, X., Wang, X.: Decadal/interdecadal variations of the ocean temperature
844   and its impacts on climate, Adv. Atmospheric Sci., 23, 964-981,
845   https://doi.org/10.1007/s00376-006-0964-7, 2006.

846 Li, Y., Curchitser, E.N., Wang, J., Peng, S.: Tidal Effects on the Surface Water Cooling
847   Northeast of Hainan Island, South China Sea, J. Geophys. Res. Oceans, 125, JC016016,
848   https://doi.org/10.1029/2019JC016016, 2020.

849 Lyard, F.H., Allain, D.J., Cancet, M., Carrère, L., Picot, N.: FES2014 global ocean tide atlas:
850   design and performance, Ocean Sci., 17, 615-649, https://doi.org/10.5194/os-17-615-
851   2021, 2021.

852 Madec, G., Bourdallé-Badie, R., Chanut, J., Clementi, E., Coward, A., Ethé, C., Iovino, D., Lea,
853   D., Lévy, C., Lovato, T., Martin, N., Masson, S., Mocavero, S., Rousset, C., Storkey,
854   D., Vancoppenolle, M., Müeller, S., Nurser, G., Bell, M., & Samson, G.: NEMO ocean
855   engine, Zenodo [10.5281], https://doi.org/10.5281/zenodo.3878122, 2019.

856 Magalhaes, J.M., da Silva, J.C.B., Buijsman, M.C., Garcia, C. a. E.: Effect of the North
857   Equatorial Counter Current on the generation and propagation of internal solitary waves
858   off the Amazon shelf (SAR observations), Ocean Sci., 12, 243-255,
859   https://doi.org/10.5194/os-12-243-2016, 2016.

860 Mei, W., Xie, S.-P., Primeau, F., McWilliams, J.C., Pasquero, C.: Northwestern Pacific typhoon
861   intensity controlled by changes in ocean temperatures, Sci. Adv., 1, e1500014,
862   https://doi.org/10.1126/sciadv.1500014, 2015.

863 Moisan, J.R., Niiler, P.P.: The Seasonal Heat Budget of the North Pacific: Net Heat Flux and
864   Heat Storage Rates (1950–1990), J. Phys. Oceanogr., 28, 401-421,
865   https://doi.org/10.1175/1520-0485(1998)028<0401:TSHBOT>2.0.CO;2, 1998.

Muller-Karger, F.E., McClain, C.R., Richardson, P.L.: The dispersal of the Amazon's water, Nature, 333, 56-59, https://doi.org/10.1038/333056a0, 1988.

Munk, W., Wunsch, C.: Abyssal recipes II: energetics of tidal and wind mixing, Deep Sea Res. Part Oceanogr. Res. Pap., 45, 1977-2010, https://doi.org/10.1016/S0967-0637(98)00070-3, 1998.

Nagai, T., Hibiya, T.: Internal tides and associated vertical mixing in the Indonesian Archipelago, J. Geophys. Res. Oceans, 120, 3373-3390, https://doi.org/10.1002/2014JC010592, 2015.

Neto, A.V.N., da Silva, A.C.: Seawater temperature changes associated with the North Brazil current dynamics, Ocean Dyn., 64, 13-27, https://doi.org/10.1007/s10236-013-0667-4, 2014.

Niwa, Y., Hibiya, T.: Estimation of baroclinic tide energy available for deep ocean mixing based on three-dimensional global numerical simulations, J. Oceanogr., 67, 493-502, https://doi.org/10.1007/s10872-011-0052-1, 2011.

Nugroho, D., Koch-Larrouy, A., Gaspar, P., Lyard, F., Reffray, G., Tranchant, B.: Modelling explicit tides in the Indonesian seas: An important process for surface sea water properties, Mar. Pollut. Bull. Special Issue: Indonesia seas management, 131, 7-18, https://doi.org/10.1016/j.marpolbul.2017.06.033, 2018.

Peng, S., Liao, J., Wang, X., Liu, Z., Liu, Y., Zhu, Y., Li, B., Khokiattiwong, S., Yu, W.: Energetics Based Estimation of the Diapycnal Mixing Induced by Internal Tides in the Andaman Sea, J. Geophys. Res. Oceans, 126, e2020JC016521, https://doi.org/10.1029/2020JC016521, 2021.

Prestes, Y.O., Silva, A.C. da, Jeandel, C.: Amazon water lenses and the influence of the North Brazil Current on the continental shelf, Cont. Shelf Res., 160, 36-48. https://doi.org/10.1016/j.csr.2018.04.002, 2018.

Richardson, P.L., Hufford, G.E., Limeburner, R., Brown, W.S.: North Brazil Current retroflection eddies, J. Geophys. Res. Oceans, 99, 5081-5093. https://doi.org/10.1029/93JC03486, 1994.

Rosenthal, Y., Boyle, E.A., Slowey, N.: Temperature control on the incorporation of magnesium, strontium, fluorine, and cadmium into benthic foraminiferal shells from Little Bahama Bank: Prospects for thermocline paleoceanography, Geochim. Cosmochim. Acta, 61, 3633-3643, https://doi.org/10.1016/S0016-7037(97)00181-6, 1997.

Ruault, V., Jouanno, J., Durand, F., Chanut, J., Benshila, R.: Role of the Tide on the Structure of the Amazon Plume: A Numerical Modeling Approach, J. Geophys. Res. Oceans, 125, e2019JC015495, https://doi.org/10.1029/2019JC015495, 2020.

Salamena, G.G., Whinney, J.C., Heron, S.F., Ridd, P.V.: Internal tidal waves and deep-water renewal in a tropical fjord: Lessons from Ambon Bay, eastern Indonesia, Estuar. Coast. Shelf Sci., 253, 107291, https://doi.org/10.1016/j.ecss.2021.107291, 2021.

Schott, F.A., Dengler, M., Brandt, P., Affler, K., Fischer, J., Bourlès, B., Gouriou, Y., Molinari, R.L., Rhein, M.: The zonal currents and transports at 35°W in the tropical Atlantic, Geophys. Res. Lett., 30(7), 1349, https://doi.org/10.1029/2002GL016849, 2003.

Sharples, J., Tweddle, J.F., Green, J.A.M., Palmer, M.R., Kim, Y.-N., Hickman, A.E., Holligan, P.M., Moore, C.M., Rippeth, T.P., Simpson, J.H., Krivtsov, V.: Spring-neap modulation of internal tide mixing and vertical nitrate fluxes at a shelf edge in summer, Limnol. Oceanogr., 52, 1735-1747, https://doi.org/10.4319/lo.2007.52.5.1735, 2007.

Sharples, J., Moore, C.M., Hickman, A.E., Holligan, P.M., Tweddle, J.F., Palmer, M.R., Simpson, J.H.: Internal tidal mixing as a control on continental margin ecosystems, Geophys. Res. Lett., 36, L23603, https://doi.org/10.1029/2009GL040683, 2009.

Silva, A., Araujo, M., Medeiros, C., Silva, M., Bourles, B.: Seasonal changes in the mixed and barrier layers in the western Equatorial Atlantic, Braz. J. Oceanogr., 53(3-4), 83-98, https://doi.org/10.1590/S1679-87592005000200001, 2005.

Smith, J.E., Smith, C.M., Vroom, P.S., Beach, K.L., Miller, S.: Nutrient and growth dynamics of Halimeda tuna on Conch Reef, Florida Keys: Possible influence of internal tides on nutrient status and physiology, Limnol. Oceanogr., 49, 1923-1936, https://doi.org/10.4319/lo.2004.49.6.1923, 2004.

Smith, K.A., Rocheleau, G., Merrifield, M.A., Jaramillo, S., Pawlak, G.: Temperature variability caused by internal tides in the coral reef ecosystem of Hanauma bay, Hawai'i, Cont. Shelf Res., 116, 1-12, https://doi.org/10.1016/j.csr.2016.01.004, 2016.

Speer, K.G., Isemer, H.-J., Biastoch, A.: Water mass formation from revised COADS data, J. Phys. Oceanogr., 25(10), 2444-2457, https://doi:10.1175/1520-0485(1995)025<2444:WMFFRC>2.0.CO;2, 1995.

Sprintall, J., Gordon, A.L., Koch-Larrouy, A., Lee, T., Potemra, J.T., Pujiana, K., Wijffels, S.E.: The Indonesian seas and their role in the coupled ocean–climate system, Nat. Geosci., 7, 487-492, https://doi.org/10.1038/ngeo2188, 2014.

Sprintall, J., Gordon, A.L., Wijffels, S.E., Feng, M., Hu, S., Koch-Larrouy, A., Phillips, H., Nugroho, D., Napitu, A., Pujiana, K., Susanto, R.D., Sloyan, B., Peña-Molino, B., Yuan, D., Riama, N.F., Siswanto, S., Kuswardani, A., Arifin, Z., Wahyudi, A.J., Zhou, H., Nagai, T., Ansong, J.K., Bourdalle-Badié, R., Chanut, J., Lyard, F., Arbic, B.K., Ramdhani, A., Setiawan, A.: Detecting Change in the Indonesian Seas, Front. Mar. Sci., 6, 257, https://doi.org/10.3389/fmars.2019.00257, 2019.

Swift, J.H., Aagaard, K.: Seasonal transitions and water mass formation in the Iceland and Greenland seas, Deep Sea Res. Part Oceanogr. Res. Pap., 28, 1107-1129, https://doi.org/10.1016/0198-0149(81)90050-9, 1981.

Tchilibou, M., Gourdeau, L., Morrow, R., Serazin, G., Djath, B., Lyard, F.: Spectral signatures of the tropical Pacific dynamics from model and altimetry: a focus on the meso-/submesoscale range, Ocean Sci., 14, 1283-1301, https://doi.org/10.5194/os-14-1283-2018, 2018.

Tchilibou, M., Gourdeau, L., Lyard, F., Morrow, R., Koch Larrouy, A., Allain, D., Djath, B.: Internal tides in the Solomon Sea in contrasted ENSO conditions, Ocean Sci., 16, 615-635, https://doi.org/10.5194/os-16-615-2020, 2020.

Tchilibou, M., Koch-Larrouy, A., Barbot, S., Lyard, F., Morel, Y., Jouanno, J., Morrow, R.: Internal tides off the Amazon shelf during two contrasted seasons: interactions with background circulation and SSH imprints, Ocean Sci., 18, 1591-1618, https://doi.org/10.5194/os-18-1591-2022, 2022.

Varona, H.L., Veleda, D., Silva, M., Cintra, M., Araujo, M.: Amazon River plume influence on Western Tropical Atlantic dynamic variability, Dyn. Atmospheres Oceans, 85, 1-15, https://doi.org/10.1016/j.dynatmoce.2018.10.002, 2019.

Vlasenko, V., Stashchuk, N.: Amplification and Suppression of Internal Waves by Tides over Variable Bottom Topography, J. Phys. Oceanogr., 36, 1959-1973, https://doi.org/10.1175/JPO2958.1, 2006.

Wang, X., Peng, S., Liu, Z., Huang, R.X., Qian, Y.-K., Li, Y.: Tidal Mixing in the South China Sea: An Estimate Based on the Internal Tide Energetics, J. Phys. Oceanogr., 46, 107-124 https://doi.org/10.1175/JPO-D-15-0082.1, 2016.

Wentz, F.J.: A 17-Yr Climate Record of Environmental Parameters Derived from the Tropical Rainfall Measuring Mission (TRMM) Microwave Imager., Journal of Climate, 28, 6882-6902, https://doi.org/10.1175/JCLI-D-15-0155.1, 2015.

963 Whalen, C.B., Talley, L.D., MacKinnon, J.A.: Spatial and temporal variability of global ocean
964   mixing inferred from Argo profiles, Geophys. Res. Lett., 39, L18612,
965   https://doi.org/10.1029/2012GL053196, 2012.
966 Xie, S.-P., Carton, J.A.: Tropical Atlantic variability: Patterns, mechanisms, and impacts, Wash.
967   DC Am. Geophys. Union Geophys. Monogr. Ser., 147, 121-142,
968   https://doi.org/10.1029/147GM07, 2004.
969 Xu, P., Yang, W., Zhu, B., Wei, H., Zhao, L., Nie, H.: Turbulent mixing and vertical nitrate
970   flux induced by the semidiurnal internal tides in the southern Yellow Sea, Cont. Shelf
971   Res., 208, 104240, https://doi.org/10.1016/j.csr.2020.104240, 2020.
972 Yadidya, B., Rao, A.D.: Projected climate variability of internal waves in the Andaman Sea,
973   Commun. Earth Environ., 3, 1-12, https://doi.org/10.1038/s43247-022-00574-8, 2022.
974 Zalesak, S.T., Fully multidimensional flux-corrected transport algorithms for fluids, J. Comput.
975   Phys., 31, 335-362, https://doi.org/10.1016/0021-9991(79)90051-2, 1979.
976 Zaron, E.D.: Baroclinic Tidal Sea Level from Exact-Repeat Mission Altimetry, J. Phys.
977   Oceanogr., 49, 193-210. https://doi.org/10.1175/JPO-D-18-0127.1, 2019.

978

979
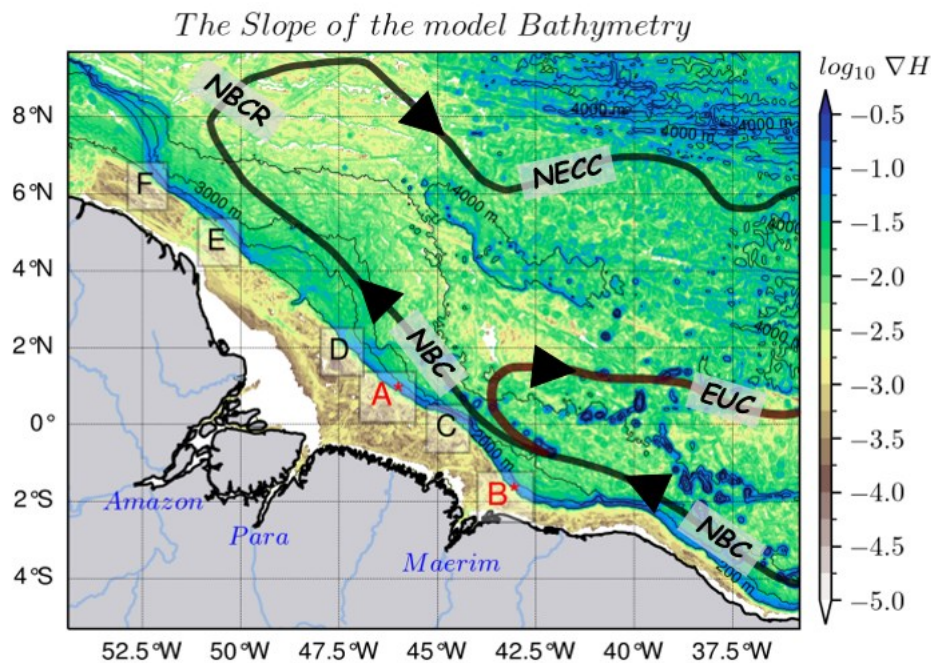
980

981 *Figure 1. The horizontal gradient of the model's bathymetry (∇H) with internal tides generation*
982 *sites (A*, B*, C, D, E and F) along the high slope of the shelf break (blue color shading), with*
983 *the two main sites A* and B* (in red), as reported in Magalhaes et al. (2016) and Tchilibou et*
984 *al. (2022). Solid bold lines represent a schematic view of the circulation (as described by*
985 *Didden and Schott, 1993; Richardson et al., 1994; Johns et al., 1998; Bourles et al., 1999a;*
986 *Schott et al., 2003; Garzoli et al., 2004) with NBC, NBCR and NECC tracks in black, and the*
987 *EUC track in brown red. Tin black contours are 200 m, 2000 m, 3000 m and 4000 m isobaths*
988 *from the model bathymetry.*

989

990

991
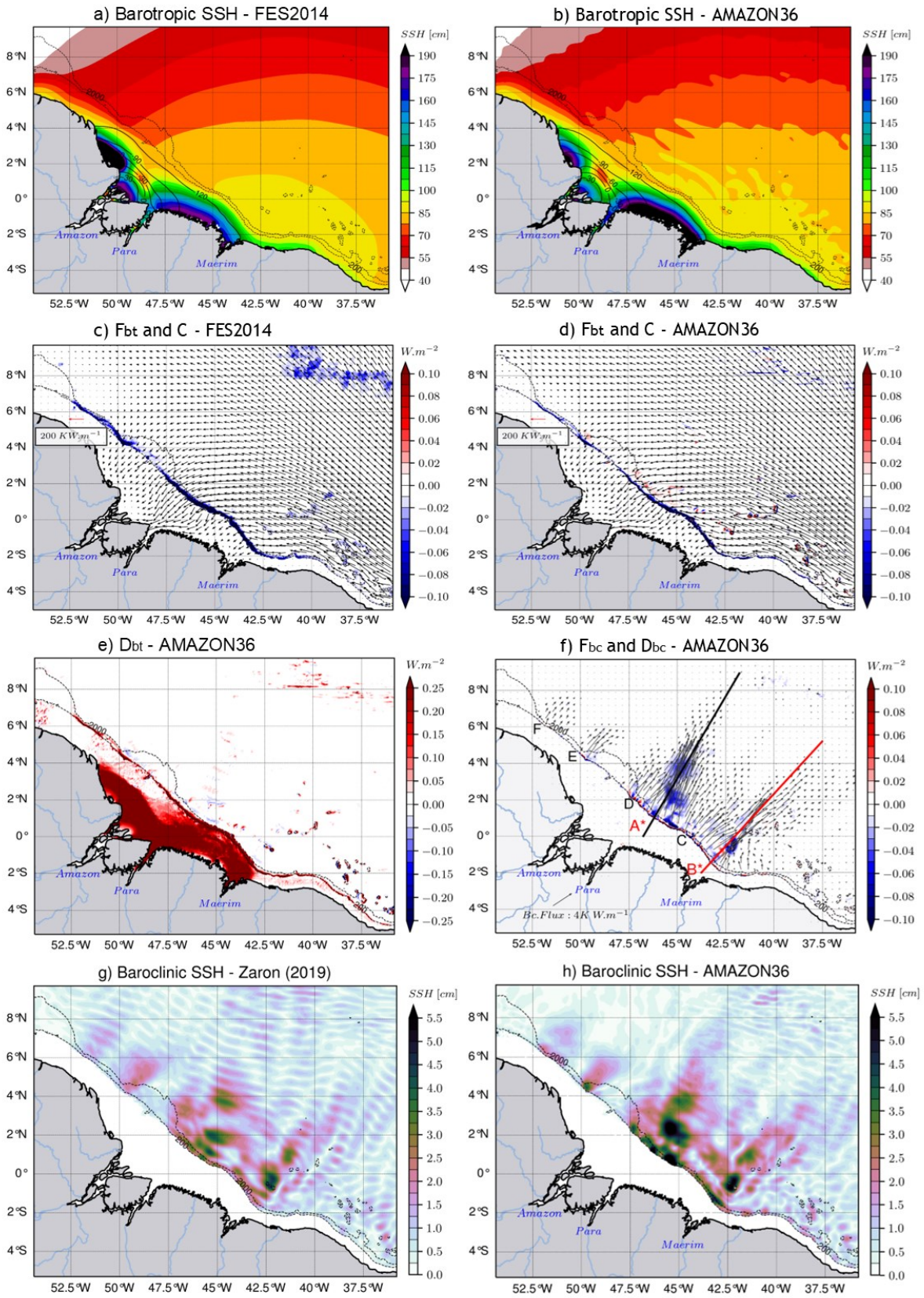
bt : barotropic ; bc : baroclinic
F : energy flux ; C : barotropic-to-baroclinic energy conversion ; D : dissipation

992
993   *Figure 2. Characteristics of M₂ coherent tides. Barotropic sea surface height (color shading)*

and its phase (solid contours) for (a) FES2014 and (b) the model, barotropic energy flux (black arrows) with the energy conversion rate (color shading) for (c) FES2014 and (d) the model, (e) the model depth-integrated barotropic energy dissipation, (f) the model depth-integrated baroclinic energy flux (black arrows) and the depth-integrated baroclinic energy dissipation (color shading) with transect lines along IT trajectories A* (black) and B* (red), the baroclinic sea surface height from (g) Zaron (2019) and (h) the model. Data from the model are the mean value over the year 2015. For all panels, dashed black contours represent the 200 m and 2000 m isobaths of the model bathymetry.
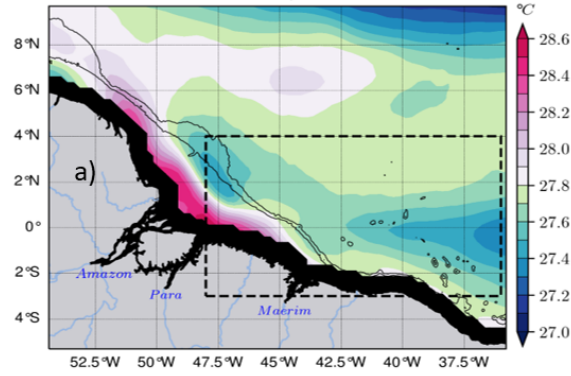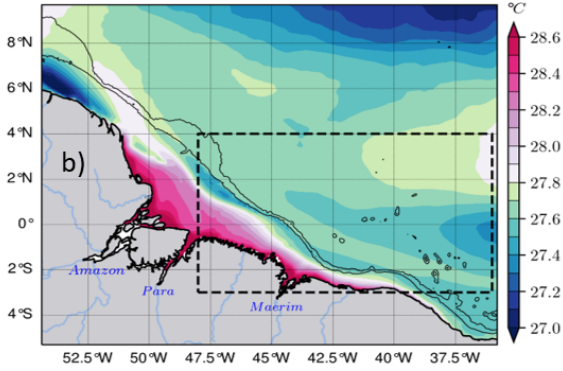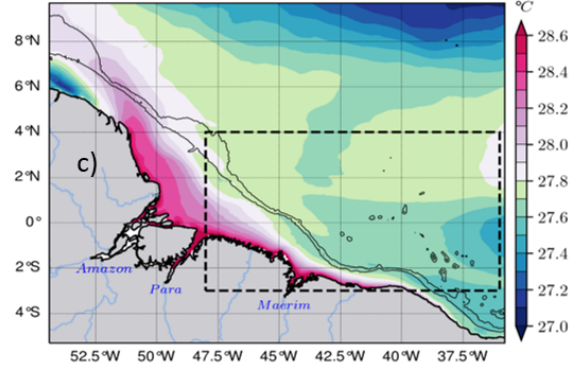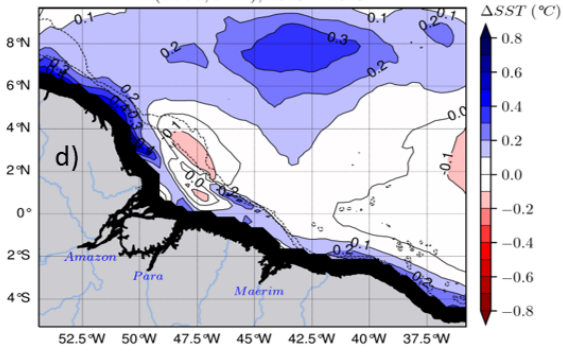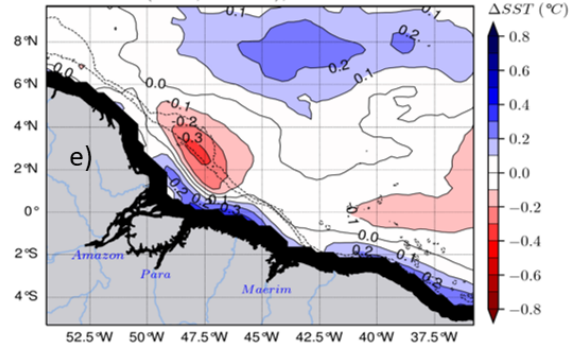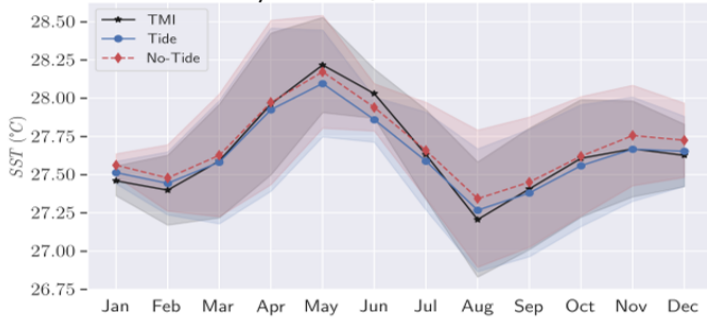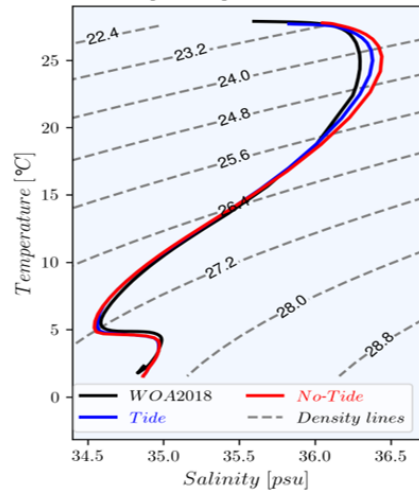
Figure 3. Validation of the model temperature for the whole period 2013-2015. Mean SST for (a) TMI with its black coastal mask, (b) the tidal simulation, (c) the non-tidal simulation, the difference (bias) in SST between TMI and (d) the tidal simulations and (e) the non-tidal simulation, (f) the seasonal cycle of the SST of the three products averaged within the dashed box in upper panels covering IT pathways with values masked below the 200 m isobath, bands indicate variability according to standard deviation. Solid black lines in panels a–c and dashed black lines in panels d–e represent the 200 m and 2000 m isobaths from the model bathymetry, while solid black lines in panels d–e represent bias contours. (g) Temperature-Salinity (T-S) diagram of the mean properties in the same area as (f) from observed WOA2018 climatology (black line), the tidal simulations (blue line) and non-tidal simulations (red line) for the water column from surface to 5500 m depth, dashed gray lines represent density (σ_θ) contours.
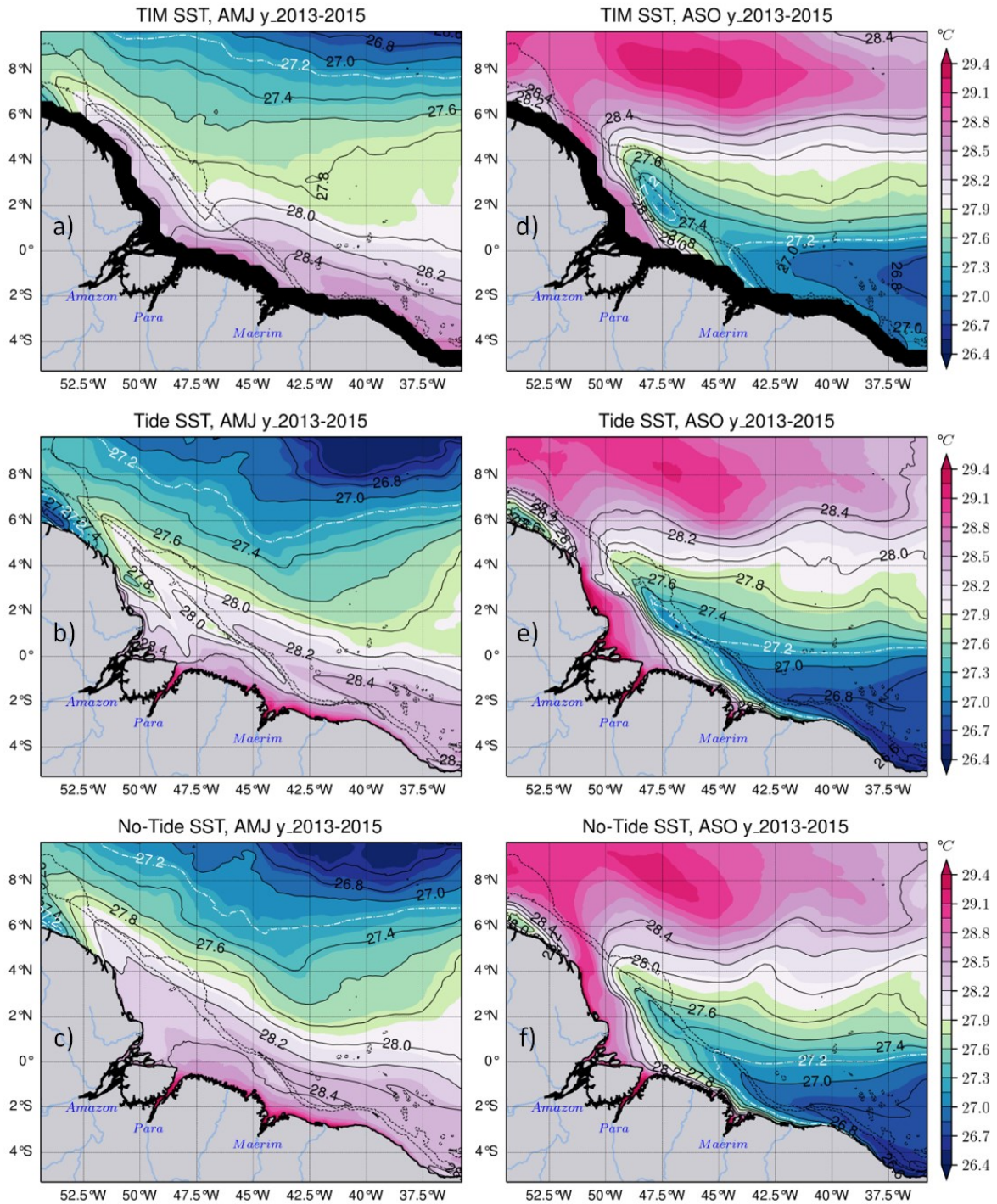
1062

Figure 4. 2013-2015 seasonal SST mean. The left panels stand for the AMJ season for TMI
with its black coastal mask, the tidal simulations and the non-tidal simulations, respectively
for the upper-left, center-left and lower-left panel; the same in the panels on the right but for
ASO season. The dashed white and black solid lines represent the temperature contours.
Dashed black lines in all panels stand for the 200 m and 2000 m isobaths from the model
bathymetry.
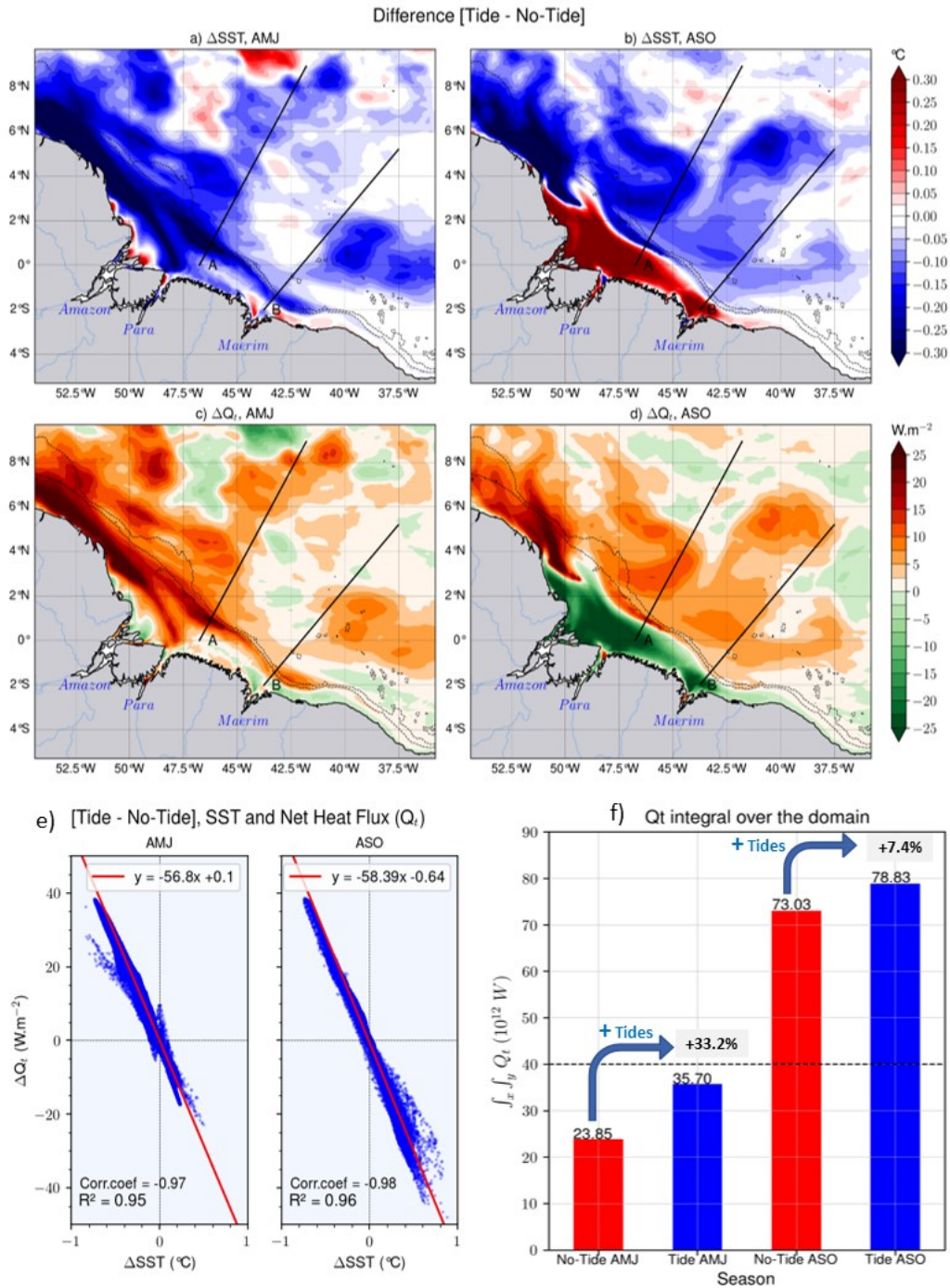
1071

Figure 5. Relationship between the SST and the atmosphere-ocean net heat flux (Qt): SST
anomaly [Tide - No-Tide] in AMJ (a) and ASO (b) seasons, Qt anomaly in AMJ (c) and ASO
(d) seasons, (e) correlation between Qt anomaly and SST anomaly for each season, (f) domain
integrated Qt for both seasons of each simulation. Dashed black lines in panels a–d stand for
the 200 m and 2000 m isobaths from the model bathymetry.

1072
1073
1074
1075
1076

1077

1078

1079

1080
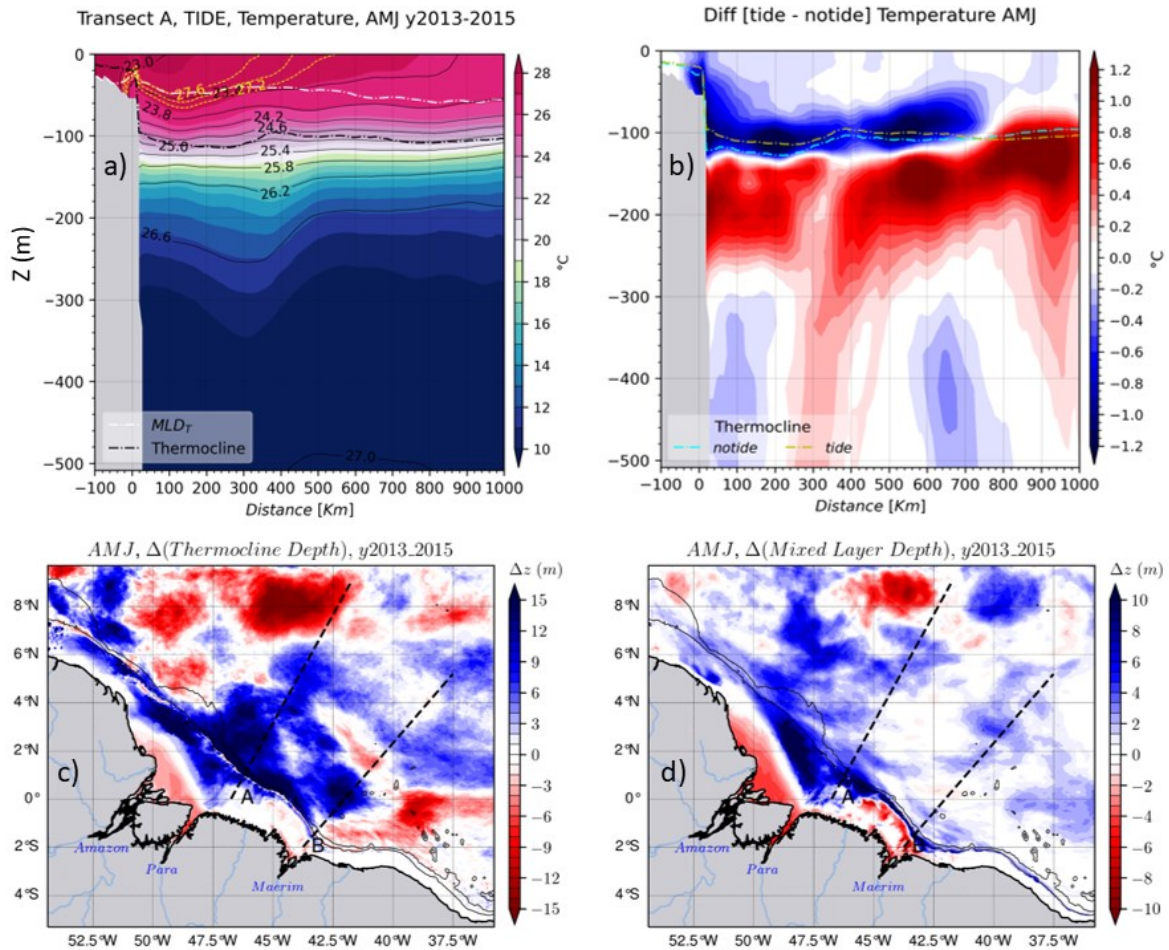
Figure 6. Water mass properties for the AMJ season: (a) vertical section of the temperature of the tidal simulations following the transect A, the yellow dashed and the solid black lines are the temperature and density (σ_θ) contours, respectively. The black and white ticker dashed lines are the thermocline and MLD, respectively. (b) the temperature anomaly for the same vertical section, yellow and cyan dashed lines are the thermocline depth for the tidal and non-tidal simulations, respectively. (c) thermocline depth anomaly and (d) MLD anomaly for the whole domain. The blue (vs red) color shading in the MLD or the Thermocline depth anomaly means that tides rise (vs deepen) them. Solid black lines in lower panels stand for the 200 m and 2000 m isobaths from the model bathymetry.
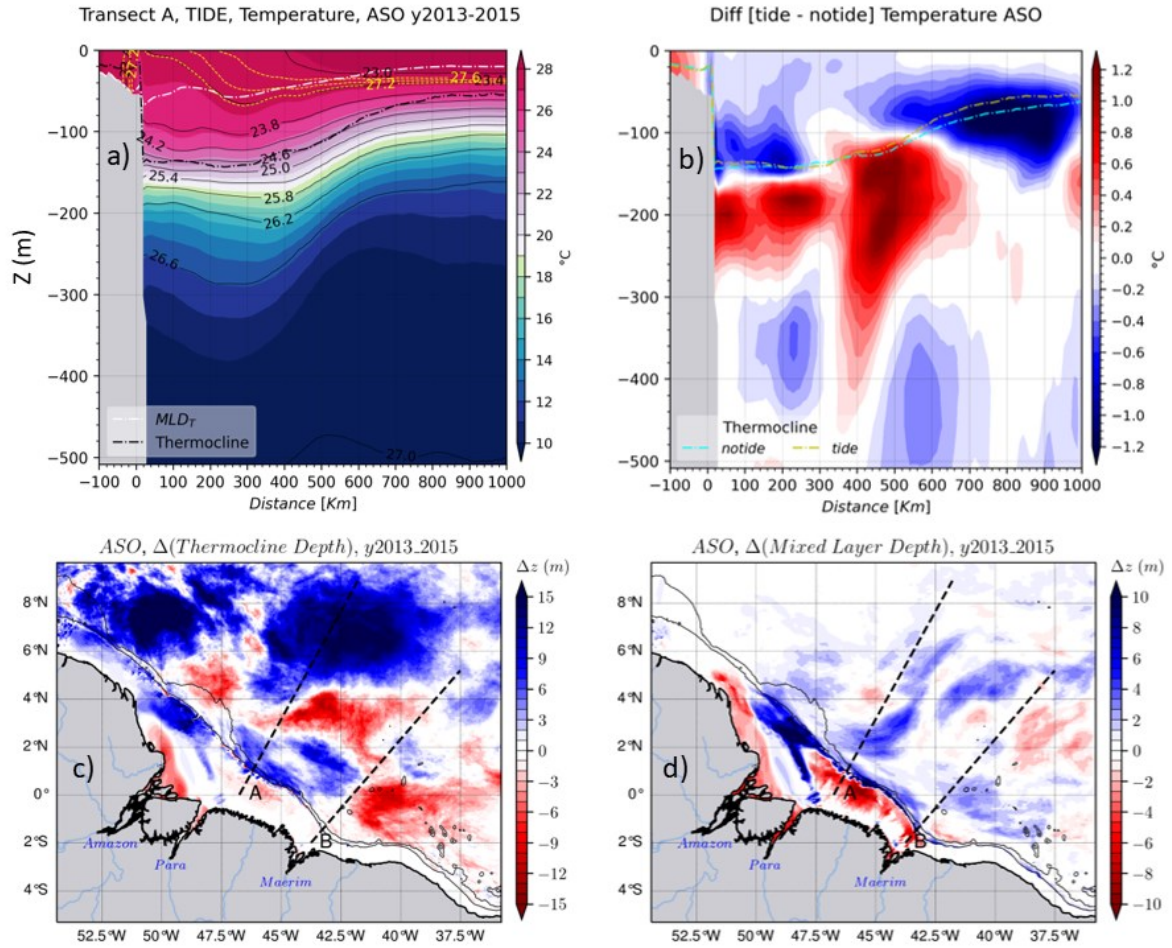
1100

1101 *Figure 7. Same as figure 6 but for ASO season.*

1102

1103

1104

1105

1106

1107

1108

1109

1110

1111

1112

1113

1114

1115
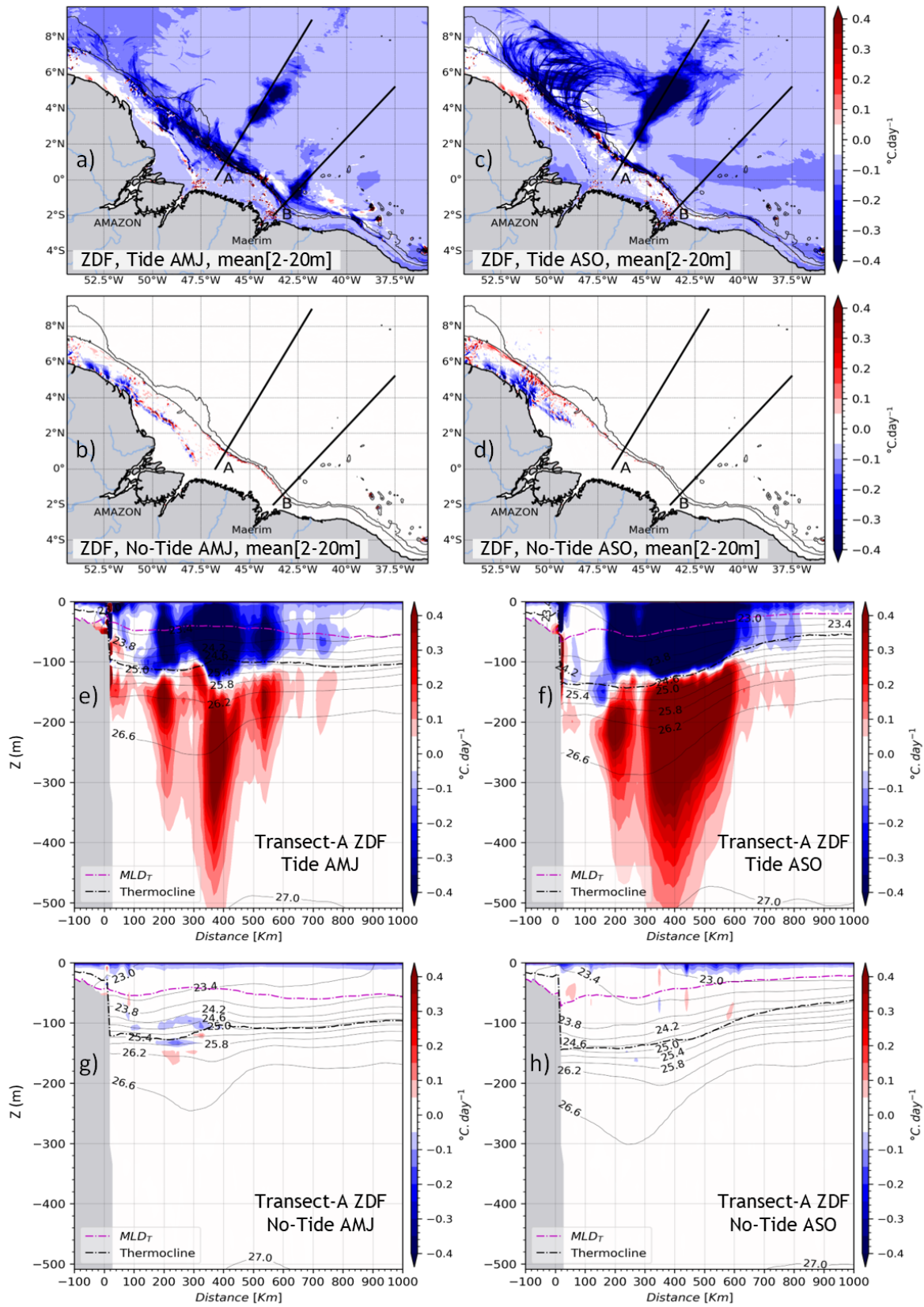
1116

Figure 8. The vertical diffusion tendency of temperature (ZDF) for both seasons. The vertical mean between 2–20 m for AMJ season in tidal (a) and non-tidal (b) simulations; then for ASO

season in tidal (c) and non-tidal (d) simulations. Vertical sections of ZDF following the transect A in the tidal simulations for (e) AMJ and (f) ASO seasons; then for the non-tidal simulations for (g) AMJ and (h) ASO seasons. Solid black lines in panels a–d stand for the 200 m and 2000 m isobaths from the model bathymetry, while they represent the density (σ_θ) contours in panels e–h. The magenta and black dashed lines in panels e–h represent MLD and the thermocline depth, respectively.

1154
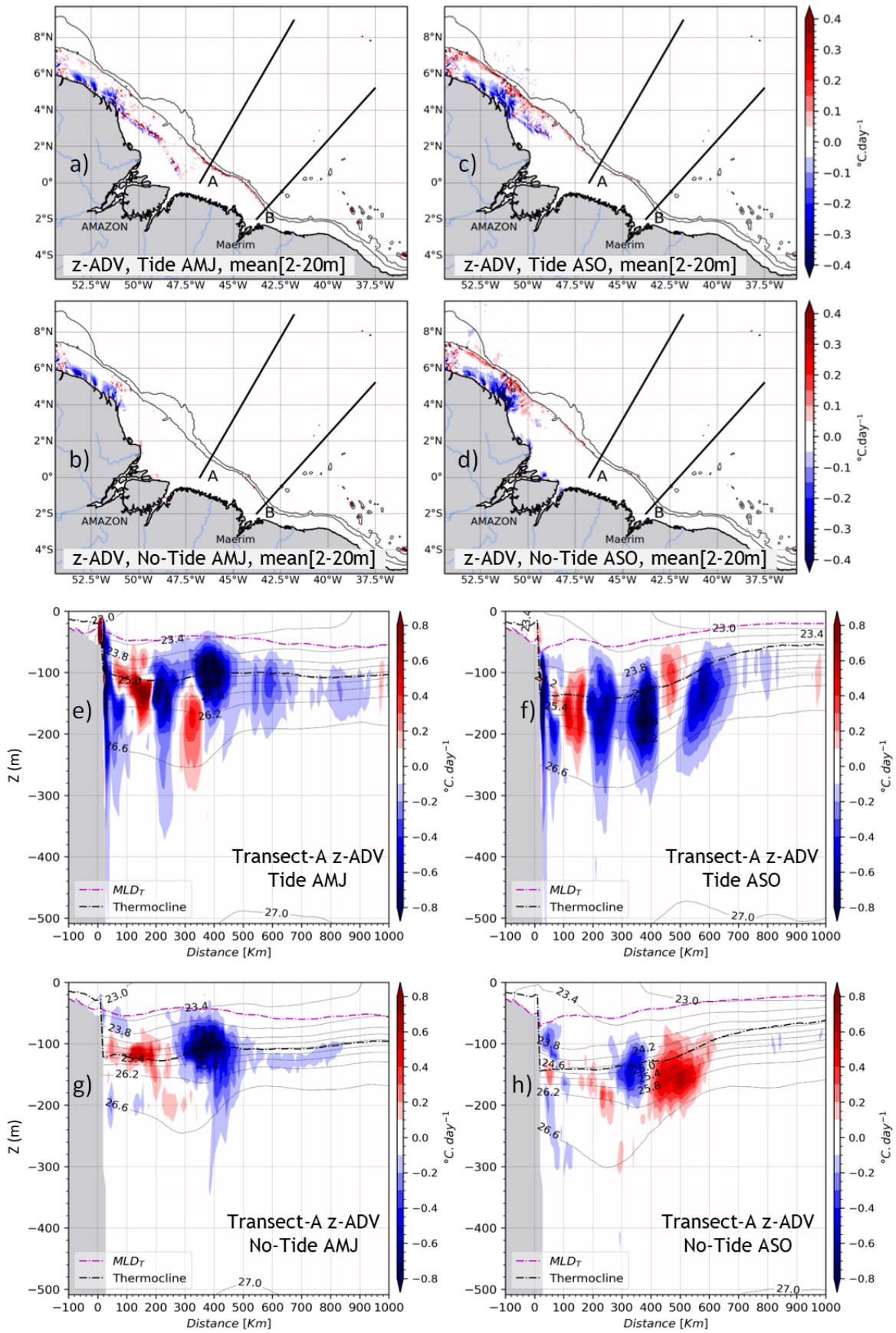
1155   *Figure 9. Same as figure 8, but for the vertical advection of temperature (z–ADV).*

1156

1157

1158

1159

1160

1161

1162

1163

1164

1165

1166

1167

1168

1169

1170

1171

1172

1173

1174

1175

1176

1177

1178

1179

1180

1181

1182

1183

1184

1185

1186

1187

1188
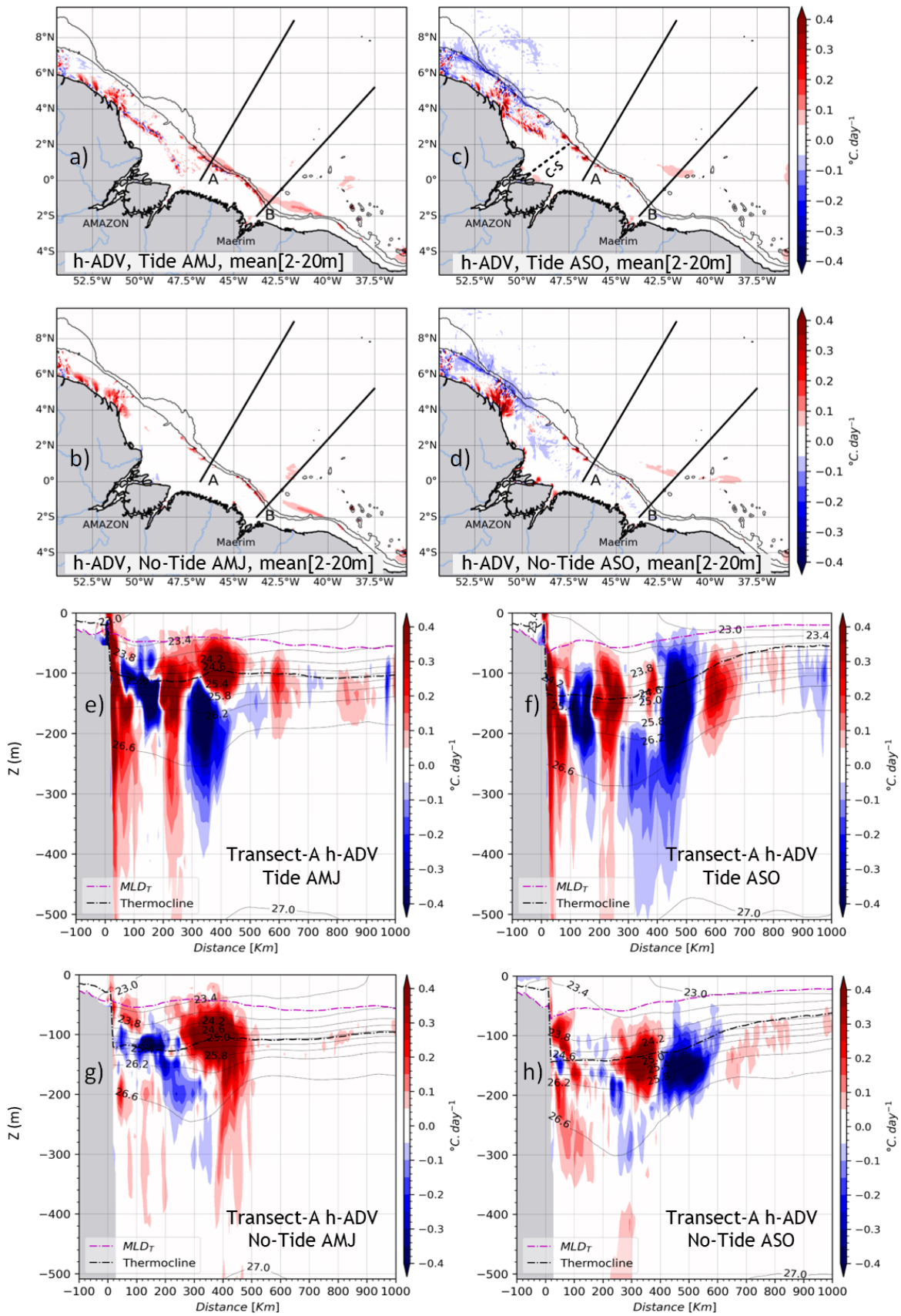
Figure 10. Same as figure 8 but for the horizontal advection of temperature (h–ADV = x–ADV + y–ADV). The dashed line from the Amazon River mouth toward the outer shelf in the panel (b) indicates the cross-shore transect (C-S) used further on.
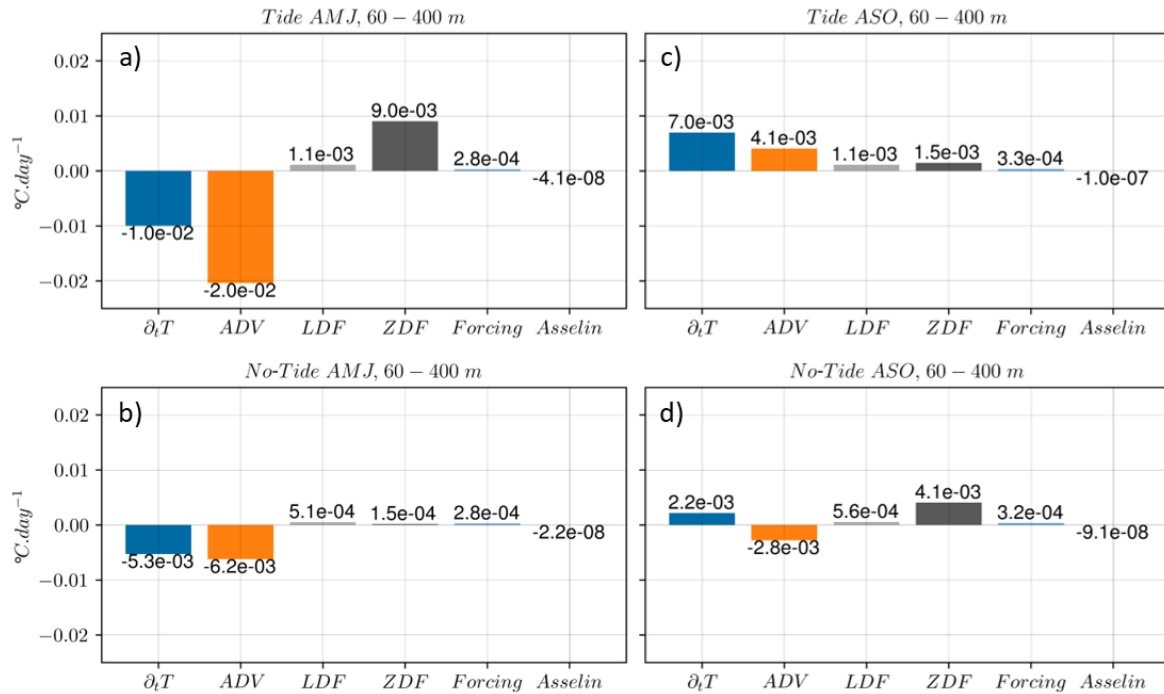
Figure 11. Three-dimensional heat budget equation terms averaged in region around IT trajectories between 48°W–40°W and 0°N–6°N, and below the MLD between 60-400 m depth. Upper panels are for the tidal simulations and lower panels for the non-tidal simulations, while left and right panels are for the AMJ and ASO seasons, respectively.
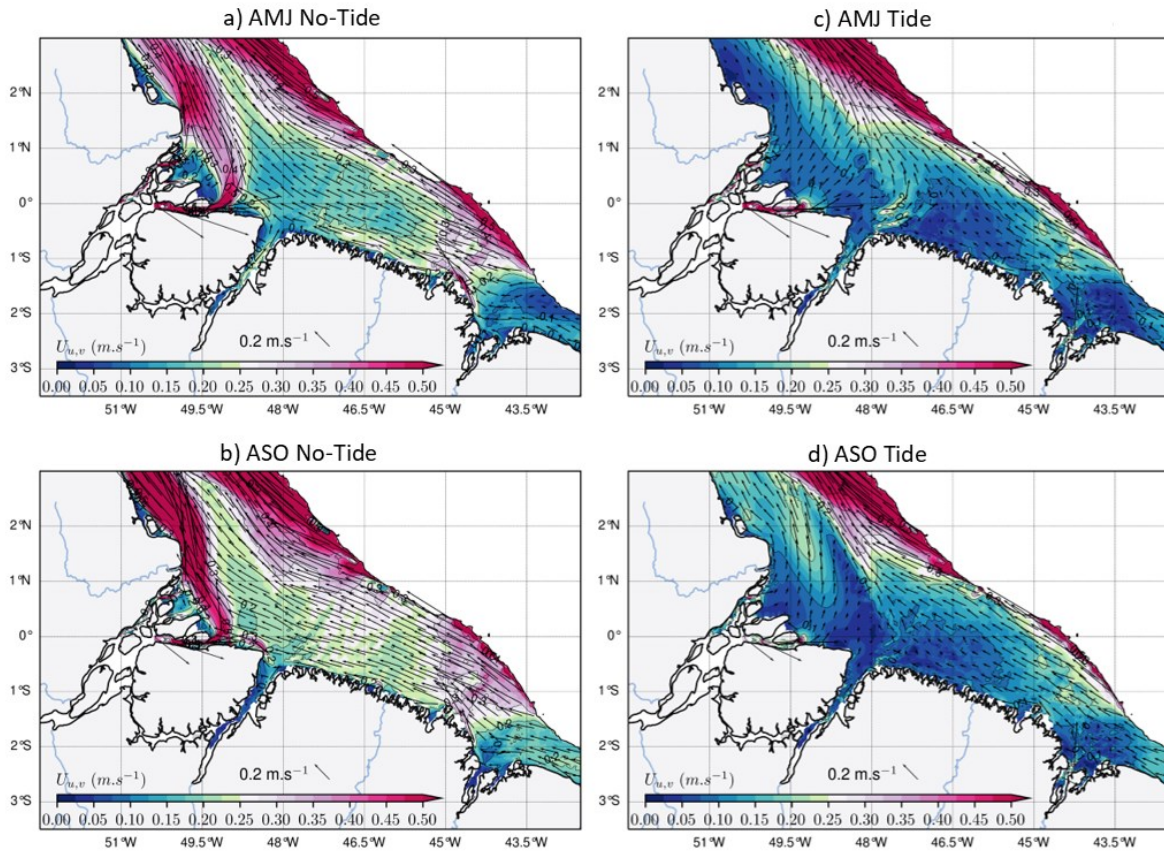
1212

1213 *Figure 12. Seasonal mean of the mean current ($U_{u,v}$) at the shelf averaged between the surface*
1214 *and 50 m: the non-tidal simulations in the left panels and the tidal simulations in the right*
1215 *panels. The upper panels stand for AMJ season, while the lower stand for ASO season. The*
1216 *color shading is the modulus of the current and the black arrows represent its direction. Values*
1217 *beyond the 200 m isobath are masked.*

1218

1219

1220

1221

1222

1223

1224

1225

1226

1227

1228

1229

1230
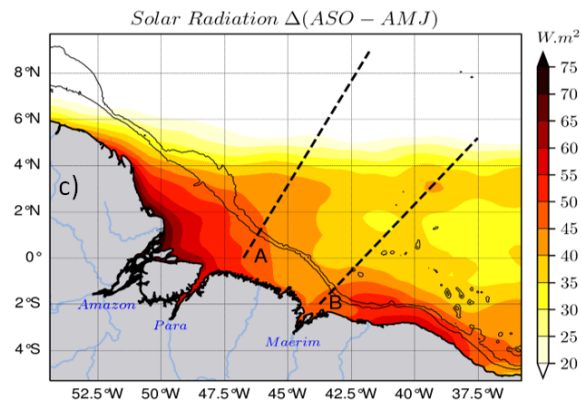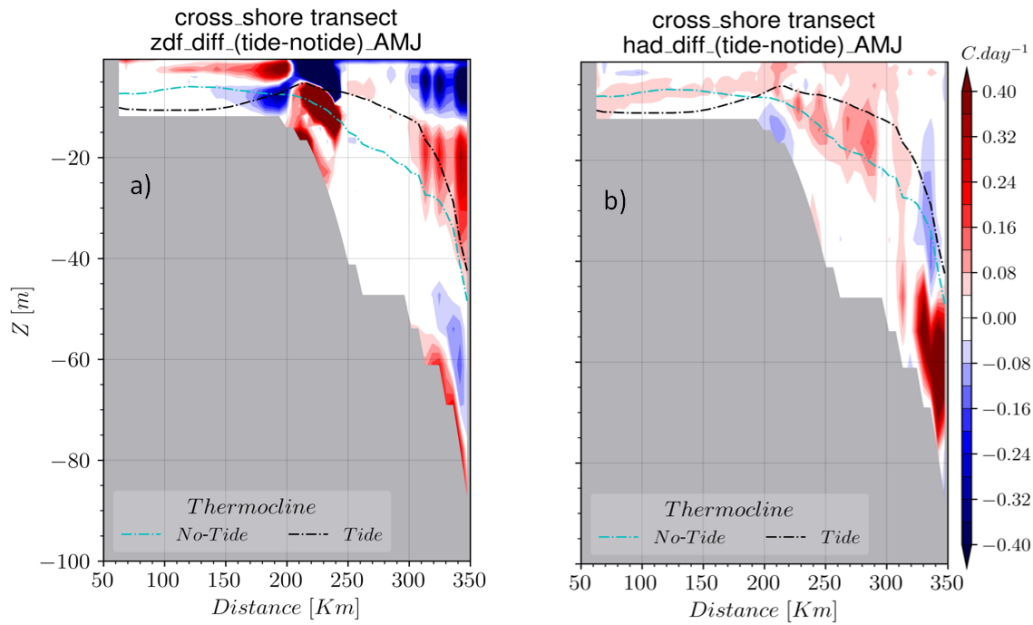
Solar radiation (Qs) increases in the ASO season:
> 30 W.m² offshore
> 60 W.m² over the shelf

1231
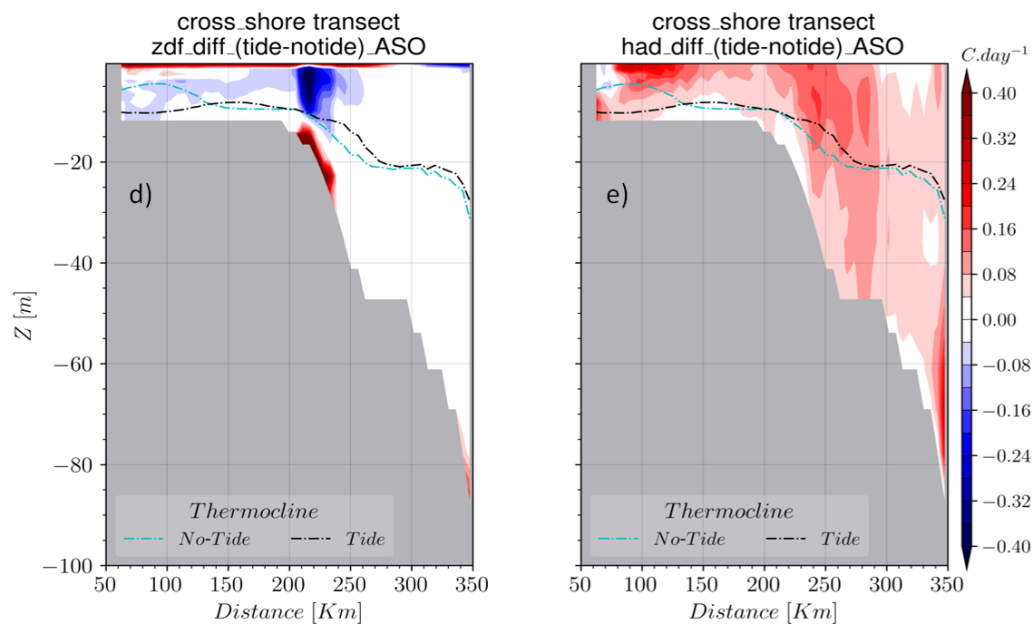
1232 *Figure 13. The cross-shore transect of ZDF anomaly for (a) AMJ and (b) ASO seasons, (c)*
1233 *difference in solar radiation between ASO and AMJ seasons. Solar radiation increases during*
1234 *the ASO season, with greater intensity on the shelf. The cross-shore transect of h–ADV anomaly*
1235 *for (d) AMJ and (e) ASO seasons.*

1236

1237

1238
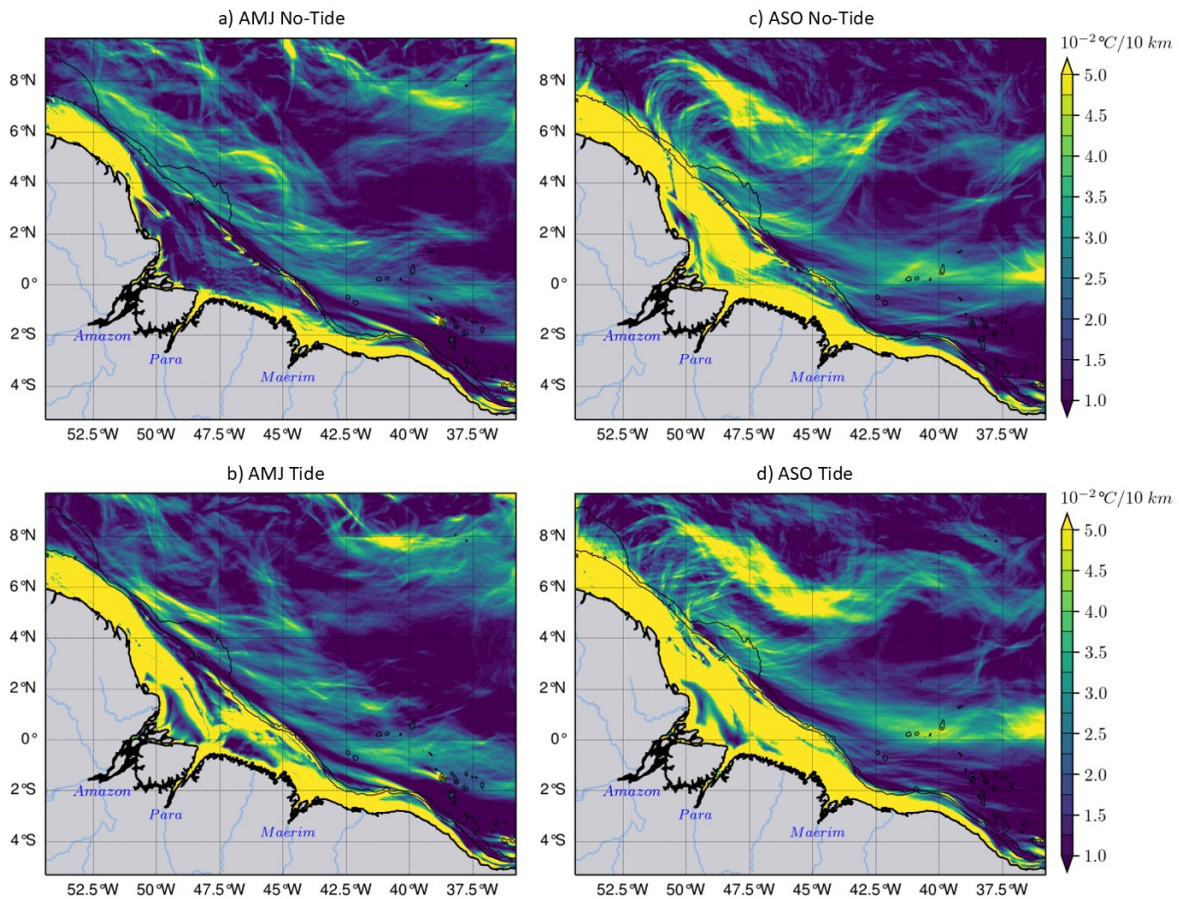
1239

1240 *Figure 14. The horizontal gradient of the Temperature (∇T) averaged between 2–20 m: the*
1241 *AMJ season in the left panels and ASO season in the right panels, the simulations without tides*
1242 *in the upper panels, and with tides in the lower panels. During the ASO season, the stronger*
1243 *NBC retroflects in the north-west and eddy activity intensifies. Therefore, ∇T emphasizes eddy-*
1244 *like fronts at the same location as eddy-like patterns in ZDF (Fig.8c).*

1245

1246

1247

1248

1249